

An improved multi-phase weakly-compressible SPH model for modeling various landslides



Youting Qi ^a, Jianyun Chen ^{a,b,*}, Guibin Zhang ^a, Qiang Xu ^{a,b}, Jing Li ^{a,b}

^a School of Hydraulic Engineering, Faculty of Infrastructure Engineering, Dalian University of Technology, Dalian 116024, China

^b State Key Laboratory of Coastal and Offshore Engineering, Dalian University of Technology, Dalian 116024, China

ARTICLE INFO

Article history:

Received 8 September 2021

Received in revised form 18 December 2021

Accepted 6 January 2022

Available online 11 January 2022

Keywords:

Granular landslides

Multi-phase WCSPH model

Particle shifting technique

Incremental diffusive term

Friction boundary condition

ABSTRACT

A novel weakly compressible multi-phase SPH method is developed for modeling various landslides. In this model, the multi-phase system of fluid and granular materials is regarded as a continuum with multi-viscosity and multi-density. The mechanical behavior of the granular materials is described by the $\mu(I)$ rheological model and the dynamic effective pressure. An incremental diffusive term is developed to eliminate the non-physical fluctuation in the pressure field of multi-phase flow. A dynamic calculation method of effective pressure is introduced to overcome the additional calculation and error caused by the traditional method in searching for the phase interface. A friction boundary condition called the momentum method is introduced to consider the influence of basal friction on the evolution of granular landslides. The Particle Shifting Technique (PST) of the single-phase WCSPH is introduced into the multi-phase WCSPH by the two-step shifting procedure to ensure the uniform distribution of particles in each phase and phase interface during the simulation process. The effectiveness of the incremental diffusive term is first validated using a benchmark case of the two phases hydrostatic stratified column. Then the model is applied to the numerical simulation of dry granular landslide, sub-aerial granular landslide, submerged granular landslide, and rigid landslide. The calculated results are compared with experimental results and previous numerical models to verify and evaluate the performance of the current model. Proven that this model is well consistent with experimental results and has higher accuracy than previous numerical models.

© 2022 Elsevier B.V. All rights reserved.

1. Introduction

The movement of granular materials in free surface flow is a common natural phenomenon. For example, landslides that located on lakes, reservoirs, bays, and oceans. Landslides and induced impulse waves are sediment transport processes that contain large amounts of granular mass. These processes are the rapid movement of large deformation, fragmentation, and frequent topological changes of dense sediments [1]. The sediment carried by the landslide will also change the topography and morphology of the damage region [2–6]. Due to their enormous energy, landslides and the induced impulse wave usually threaten critical infrastructure and human life. Therefore, accurate prediction of the movement of granular materials in free surface flow is critical for hazard prevention and mitigation assessment [7].

Physical model tests and numerical simulations are effective tools for researchers to understand and study these challenging areas. Because the majority of the experiment test models are small-size, some

physical characteristics of landslides cannot be captured [2]. In contrast, numerical simulation has remarkable advantages in reducing costs and surpassing the limitations of physical tests research. The numerical method of granular material motion is mainly based on the continuous or discrete description of granular material [1,8,9]. Discrete description, for instance, the discrete element method, describes the problem on a particle scale. However, for a numerical model containing millions of particles, the required computing resources are costly, and it is challenging to solve the actual scale problem [8,9]. Different from the discrete description, the continuum description (such as mesh-based or meshless particle methods) regards granular materials as a continuum medium and predicts the state of the flow system by solving the conservation equation. The continuum description can solve broader problems, so it has been used in many numerical studies in the past [5,8,10].

The mesh-based continuum methods have been successfully applied to the description of granular materials [9,11–13]. However, these methods may encounter difficulties in handling the deformation and fragmentation of the interface after the failure of granular flows [1]. The mesh-free particle methods can overcome these difficulties encountered by the mesh-based methods, such as the most commonly used SPH [14] and MPS [15]. SPH is a Lagrangian mesh-free method

* Corresponding author at: School of Hydraulic Engineering, Faculty of Infrastructure Engineering, Dalian University of Technology, Dalian 116024, China.

E-mail address: chenjydg@dlut.edu.cn (J. Chen).

proposed by Lucy [16] to study astrophysical applications and was later extended by Monaghan [17] to handle free surface problems. It was then widely used in numerical simulation of fluid-solid coupling dynamics [18–23], free surface flow [24–27], and multi-phase flow problems [24,28].

The SPH method is more accessible than Eulerian methods to model the interface between two phases and fluid and the free surfaces, so it has been widely utilized in granular flow [29], including granular landslide [29–32], movable-bed scouring [29,30,33–35], and granular collapse [29–31,33,36]. Most of the current theoretical research and numerical simulations are dedicated to the research of versatile and reliable constitutive models to better simulate various forms of dense granular flow [37–39]. Nowadays, several rheological models have been developed, such as the Newtonian model [40], elastoplastic soil model [41]. Additionally, some different generalized visco-plastic models (non-Newtonian fluid) are also developed, including Bingham [34], Herschel-Bulkley [2], Cross model [42], and Visco-inertial model [43]. Recently, close attention has been paid to the $\mu(I)$ rheological model, which is specially used for granular materials [8,29,37,44–49]. The rheological properties of this model are closely relevant to the physical properties of materials, and the granular flow regimes are also considered [48].

In these rheological models, it is crucial to accurately estimate the normal stress (i.e., effective pressure) in the solid skeleton for detecting the yield and non-yield flow regions. In this respect, the hydrostatic assumption is commonly used in calculating pore water pressure in the rheological model [38,50]. However, the lithologic assumptions used to calculate pore water pressure usually require detecting free surfaces and interfaces in advance. In addition, the hydrodynamic characteristics in the motion of granular flow are ignored in the calculation of the effective pressure. This limits the ability of sophisticated particle methods to handle highly deformed interfaces in immersed granular flow. Regarding the problem above, Zubeldia et al. [51] and Fourtakas and Rogers [52] estimated the pore water pressure using the density of saturated sediments and adopted the modified equation of state (EOS). However, different reference pressures (total pressure and pore water pressure) in EOS are considered in their model, and pressure fluctuations arising from slight compressibility will affect the sediment model overestimating the viscosity in submerged conditions [50]. Jandaghian et al. [38] proposed a consistent method for calculating effective pressure in the framework of weakly compressible MPS. Based on the law of mass conservation of pore water in the mixture phase, this method dynamically updates the pore water pressure field of the mixture phase without interface detection. Also, it includes the hydrodynamics properties of fluid flow.

In addition, the false pressure oscillations caused by numerical and approximation errors in the particle methods have a remarkable impact on the accuracy of the results. In recent years, many strategies have been developed to eliminate these non-physical pressure noises, such as the artificial diffusive terms [53,54], particle shifting algorithm [55,56], and higher-order particle interpolation [54,57], and to ensure stable and reliable results. Generally, adding a numerical diffusive term to the continuity equation can effectively eliminate high-frequency pressure fluctuations [38]. However, owing to the density field in the multi-phase flow being discontinuous, the artificial diffusive term at the fluid phase interface needs special treatment. To overcome these numerical problems, Fourtakas and Rogers [58] deal with the multi-phase flow problem by restricting the traditional diffusive term to particles in the same phase. In this case, the renormalization matrix and the first-order density gradient operator are also restricted to the same phase particles. Krimi et al. [31] proposed a modified version of the diffusive term for the multi-phase model to reduce false pressure caused by the assumption of weakly compressible flow; however, this model can not guarantee mass conservation. In addition, this model lacks a high-order correction term for the kernel truncation error at the interface [38]. Zheng and Chen [59] presented a multi-phase SPH model with low numerical diffusion by adopting the increments form of density.

In the SPH method, most studies on granular flow did not consider the effect of basal friction [60]. The simulation of PFEM by Zhang et al. [61,62] shows that the basal friction considerably influences the collapse morphology of granular columns. For the friction boundary condition, Gutfraind and Savage [63] presented a Coulomb-based friction boundary condition by estimating the normal repulsive force and the tangential force proportional to the normal force exerted on SPH particles from the boundary. Wang and Chan [64] proposed two contact algorithms in the SPH framework based on the ideal plastic collision assumption: penetration method and momentum method. Sheikh et al. [60] presented a correction approach according to Wang and Chan [64] that can consider the energy and friction dissipation when the granular mass contacts the solid boundary.

In this paper, a robust and accurate multi-phase WCSPH method based on the $\mu(I)$ rheological model is proposed for the numerical simulation of dry landslide, submerged, and sub-aerial granular landslide. The model is also able to deal with rigid landslides. The incremental diffusive term is proposed by adopting the incremental form of the density, which deals with the pressure oscillation issues caused by density discontinuity and enhances the robustness of the model. Moreover, based on the single-phase numerical techniques, the PST of the multi-phase flows is developed by adopting the two-step shifting procedure. Here, we introduced the ideas of Jandaghian et al. [38] into the SPH framework and proposed a dynamic effective pressure calculation method. In addition, a friction boundary condition is introduced into the model that aims to consider the influence of basal friction for predicting the evolution of the granular landslides. Several benchmark cases are used to investigate and validate the effectiveness and accuracy of the proposed model.

This paper is arranged as follows. The governing equations of multi-phase WCSPH, the SPH discrete forms, the rheological model of granular materials, and some numerical techniques of multi-phase WCSPH are described in Section 2. The boundary conditions are introduced in Section 3. A set of benchmark tests used to validate the model developed in this work include two phases hydrostatic stratified column (-Section 4.1), rigid landslide (Section 4.2), dry granular landslide (Section 4.3), submerged granular landslide (Section 4.4), and sub-aerial granular landslides (Section 4.5). The main conclusions and novelties are presented in Section 5.

2. WCSPH for multi-phase granular flows

In the multi-phase flow problem simulated by the SPH method, the water-granular mixture is usually regarded as a continuous medium, and the ambient fluid (water) is viewed as another continuous medium. These two different media constitute a system of two-phase flow. As shown in Fig. 1, Fig. 1 (a) - (c) represents the process of continuum approximation and SPH discretization. As shown in Fig. 1(a), the mixture is composed of solid particles and pore water, and the volume fraction ϕ is used to express the proportion of solid particles in the mixture per unit volume, that is, $\phi = V_s/V$. Therefore, after continuous approximation (Fig. 1(b)), the density of the mixture phase $\rho_{0m} = (1 - \phi)\rho_{0w} + \phi\rho_s$ can be determined according to the volume fraction [38], and the dynamic behavior of the mixture phase is described with a rheological model. In the SPH model, the water phase and the mixture phase are discretized into particles with the same volume, i.e., water particles and mixture particles (Fig. 1(c)). They have different masses, densities, and rheological behaviors. And this density difference is also the main reason that drives the mixture to move in the water body.

2.1. Governing equations

The governing equation of multi-phase granular flows system based on the weakly compressible model in the Lagrangian framework,

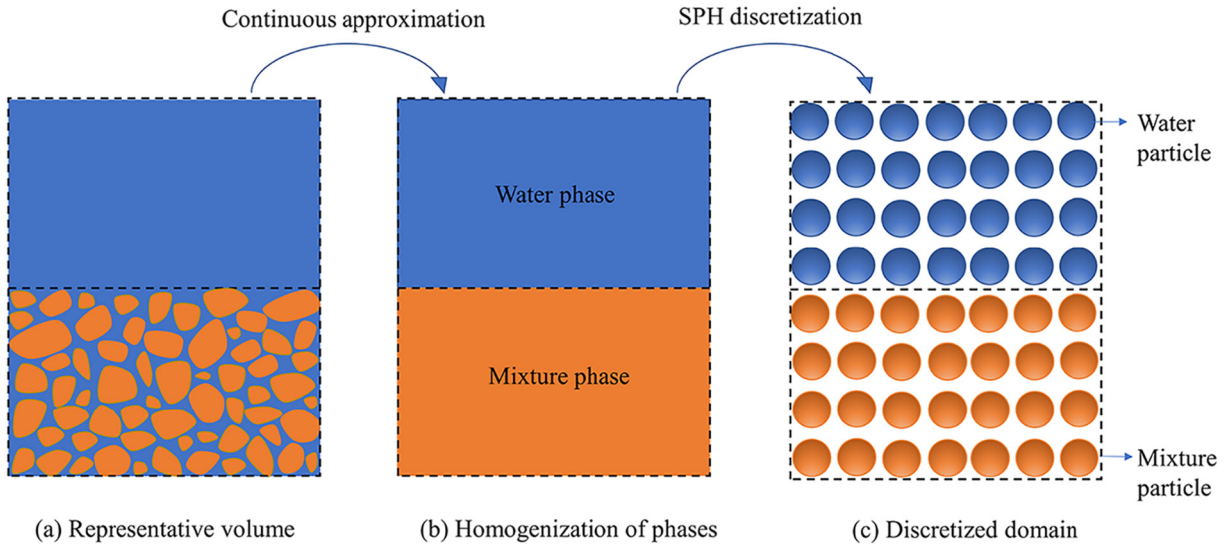


Fig. 1. Schematic of continuous approximation and discrete process of the water-granular mixture medium.

including the mass and momentum conservation equation, the equation of state, and material motion. The expressions are:

$$\begin{cases} \frac{D\rho}{Dt} + \rho \nabla \cdot \mathbf{u} = 0 \\ \frac{D\mathbf{u}}{Dt} = \frac{1}{\rho} \nabla \cdot \mathbf{T} + \mathbf{g} \\ \frac{D\mathbf{r}}{Dt} = \mathbf{u} \\ p = f(\rho) \end{cases} \quad (1)$$

where, \mathbf{u} , ρ , \mathbf{g} , and t represent the velocity vector, density, gravity vector, and time, respectively. p represents the thermodynamic pressure, which is predicted by EOS [65] for a weakly compressible assumption. \mathbf{r} represents the position vector, which is computed by the material motion in Lagrange coordinate system. \mathbf{T} is the Cauchy symmetric total stress tensor, for the viscous compressible fluid, it is as follows:

$$\mathbf{T} = -p\mathbf{I} + \boldsymbol{\tau} \quad (2)$$

and $\boldsymbol{\tau}$ denotes the shear stress tensor expressed as:

$$\boldsymbol{\tau} = 2\eta\mathbf{E} + \xi(\nabla \cdot \mathbf{u})\mathbf{I} \quad (3)$$

and strain rate tensor $\mathbf{E} = 0.5(\nabla \mathbf{u} + (\nabla \mathbf{u})^T)$. η denotes the effective viscosity for the granular materials determined by the rheological model and $\eta = \eta_f$ is the physical viscosity of the fluid. ξ is the second viscosity coefficient, which combines all viscous effects related to the volumetric strain rate [1]. For a weakly compressible fluid, it can be considered that $\nabla \cdot \mathbf{u} = 0$, the stress tensor hence is simplified to $\boldsymbol{\tau} = 2\eta\mathbf{E}$. Considering that the multi-phase system of fluid and granular materials is regarded as a continuum with multi-viscosity and multi-density, it can share a set of governing equations (system (1)) and no additional interfacial force is required [48].

2.2. SPH fundamentals

In the SPH model, the fluid region is discretized into a finite number of uniformly distributed particles; each carries field variables, including volume, density, pressure, velocity, etc. Their motion is driven by the pressure gradient and the viscous force. The field function $f(\mathbf{r})$ of the particle and its spatial derivatives $\nabla f(\mathbf{r})$ and divergence $\nabla \cdot f(\mathbf{r})$ at position \mathbf{r} are approximated through the convolution sum. The aforementioned process is known as particle approximation [66,67]. The

particle approximation formulas commonly used in the SPH model are given by:

$$\begin{cases} f(\mathbf{r}_i) = \sum_j f(\mathbf{r}_j) W(\mathbf{r}_i - \mathbf{r}_j, h) V_j \\ \nabla_i f(\mathbf{r}_i) = \sum_j [f(\mathbf{r}_i) + f(\mathbf{r}_j)] \nabla_i W(\mathbf{r}_i - \mathbf{r}_j, h) V_j \\ \nabla_i \cdot f(\mathbf{r}_i) = \sum_j [f(\mathbf{r}_i) - f(\mathbf{r}_j)] \cdot \nabla_i W(\mathbf{r}_i - \mathbf{r}_j, h) V_j \end{cases} \quad (4)$$

where the subscripts i and j represent the concerned particle and the neighboring particle in the support domain; $V_j = m_j/\rho_j$ is the volume of particle j , in which m_j and ρ_j denote the mass and density of particle j , respectively.

The selection of kernel function $W(r_i - r_j, h)$ (hereinafter referred to as W_{ij}) greatly affects the stability, efficiency, and accuracy of this model. The W_{ij} should be selected as an even function and satisfy the compact condition, delta function property, and normalization condition [20]. According to the research results of Dehnen and Aly [68], the Wendland C2 kernel function is adopted in this work [69].

$$W(q, h) = a_D \begin{cases} (1+2q)\left(1-\frac{1}{2}q\right)^4 & 0 \leq q \leq 2 \\ 0 & q \geq 2 \end{cases} \quad (5)$$

where $q = \|\mathbf{r}_i - \mathbf{r}_j\|/h$ denotes the radius of the support domain. h represents the smoothing length; $h = 2\Delta x$, $a_D = 7/(4\pi h^2)$ in 2D, $h = 1.5\Delta x$, $a_D = 21/(16\pi h^3)$ in 3D, Δx denotes the initial particle spacing.

2.3. Discrete form

In the present work, the physical domain Ω (composed of fluid phase Ω_f and granular phase Ω_g) of the multi-phase granular flows is regarded as a single multi-viscosity and multi-density continuum [8]. Therefore the entire flow field can be solved uniformly using system (1). In the multi-phase WCSPH model, the ambient fluid is discretized by the fluid-type particles, and the granular materials are represented by granular-type particles. It should be noted that when the granular materials are submerged, the granular-type particles include grains and interstitial fluid between grains. This means that the particle size Δx of the SPH must be larger than the diameter d_s of the grains.

2.3.1. Discretization of the continuity equation

The instability of the pressure field is a significant cause hindering the progress of the traditional WCPH method. Antuono et al. [54] and Marrone et al. [66] effectively eliminate high-frequency numerical noise by adding a diffusive term in the continuity equation. The discrete form of SPH of Eq. (1) is as follows:

$$\frac{D\rho_i}{Dt} = -\rho_i \sum_j (\mathbf{u}_j - \mathbf{u}_i) \cdot \nabla_i W_{ij} V_j + \delta h c_0 \sum_j \psi_{ij} \cdot \nabla_i W_{ij} V_j \quad (6)$$

where δ is recommended to be equal to 0.1. Because the traditional WCPH method can cause numerical pressure oscillation, Molteni and Colagrossi [70] introduced the standard artificial diffusive term (i.e., the last term in Eq. (6)) to remove these false oscillations in the pressure field. The expression of ψ_{ij} is as follows:

$$\psi_{ij} = 2(\rho_i - \rho_j) \frac{\mathbf{x}_{ij}}{|\mathbf{x}_{ij}|^2} \quad (7)$$

However, as the kernel function is truncated near the free surface, the standard form of the diffusive term will lead to non-physical divergence of the pressure field on the free surface. In the study of Antuono et al. [54], the convergence of the standard diffusive term is achieved by using higher-order Laplacian to eliminate the truncation error near the free surface and solid boundary. Subsequently, the model was named the δ -SPH model [66]. This form has been widely used in single-phase flow [71–73].

The numerical noise caused by density discontinuity at the interface in multi-phase flow has been solved by some strategies. One approach uses diffusive terms in different phases to avoid numerical problems at the interface [52]. However, in this way, the kernel function is truncated at the interface, resulting in the divergence of the density field [31]. Even though the higher-order Laplacian formula can reduce the related error, it is still unsuitable for highly deformable interfacial flow [38].

Similar to the method of Zheng and Chen [59], here we also adopt the form of density increment. Because this incremental form is independent of the density field, it overcomes the limitation of discontinuity of the density field and can be directly applied to the whole flow field. The detailed derivation process of the incremental diffusion term is as follows.

According to Antuono et al. [54], we define the general form of the artificial diffusive term D^{0^m-SPH} . For particle i , it is expressed as follows:

$$D_i^{0^m-SPH} = \delta h c_f \nabla^2 \rho_i \quad (8)$$

Using relational expressions $\rho_i = \rho_{i0} + \delta \rho_i$, Eq. (8) is expressed in the form of density increment:

$$D_i^{0^m-SPH} = \delta h c_f \nabla^2 (\rho_{i0} + \delta \rho_i) \quad (9)$$

Among them, $\delta \rho_i$ denotes the instantaneous density increment of particle i , ρ_{i0} denotes the initial density of particle i , which remains unchanged during the numerical simulation, that is, $\nabla^2 \rho_{i0} = 0$. Therefore, Eq. (9) can be simplified as:

$$D_i^{0^m-SPH} = \delta h c_f \nabla^2 (\delta \rho_i) \quad (10)$$

Therefore, according to Antuono et al. [54], the convergence form of the Laplacian series and Taylor series are used to discretize the above formula and obtain the incremental expression form of ψ_{ij} :

$$\psi_{ij} = 2(\delta \rho_i - \delta \rho_j) \frac{\mathbf{x}_{ij}}{|\mathbf{x}_{ij}|^2} - [\langle \nabla(\delta \rho) \rangle_i^L + \langle \nabla(\delta \rho) \rangle_j^L] \quad (11)$$

The symbol $\langle \nabla(\delta \rho) \rangle_i^L$ is the renormalized incremental density gradient, which is expressed as follows:

$$\langle \nabla(\delta \rho) \rangle_i^L = \sum_j (\delta \rho_j - \delta \rho_i) \mathbf{L}_i \nabla_i W_{ij} V_j, \quad \mathbf{L}_i = \left[\sum_j \mathbf{x}_{ji} \otimes \nabla_i W_{ij} V_j \right]^{-1} \quad (12)$$

Eq. (10) eliminates the effect of discontinuity of density field on the diffusive term. Notably, the diffusive term in the form of incremental density overcomes the dependence on the virtual particle density at the boundary. Therefore, the contribution of boundary virtual particles can be added to the higher-order term of the multi-phase flow diffusive term to overcome the pressure divergence near the boundary. For the boundary particle j , we can use the pressure p_j (see boundary method) to deduce its density increment $\delta \rho_j = p_j/c_f^2$ according to the linear equation of state [70]. When the flow field is single-phase flow, Eq. (11) degenerates to the traditional formula of single-phase diffusive term.

In the current model, the viscosity of granular material is obtained through the $\mu(I)$ rheological model. A parameter called particles volume fraction ϕ_p is needed when calculating the bulk density of granular materials, which describes the volume fraction of granular-type particles [1], and is given by (for particle i):

$$(\phi_p)_i = \frac{\sum_{j \in \Omega_g} W_{ij} V_j}{\sum_{j \in \Omega} W_{ij} V_j} \quad (13)$$

The volume fraction of grains is given by $(\phi_g)_i = \phi_0 (\phi_p)_i$, where ϕ_0 represents the initial concentration of grains. The continuous density field of the whole calculation area is defined as follows [1]:

$$\rho_i = (\phi_g)_i \rho_g + (1 - (\phi_g)_i) \rho_f \quad (14)$$

This method smoothes the sharp density changes near the phase interface, and the corresponding initial density field is defined as follows:

$$\rho_0 = \begin{cases} \phi_0 \rho_g + (1 - \phi_0) \rho_f & i \in \Omega_g \\ \rho_f & i \in \Omega_f \end{cases} \quad (15)$$

where ρ_g, ρ_f are the density of grains and the ambient fluid.

2.3.2. Discretization of momentum equation

Hu and Adams [74] developed a discretization scheme of momentum equation for multi-phase flow simulation, which only uses adjacent particles' velocity, position, volume, pressure, and viscosity. The advantage of this scheme is that although the density ratio is large, the fluid with higher density has enough influence on the lighter fluid, so it is widely used. The discretization scheme of Eq. (2) is as follows:

$$\frac{D\mathbf{u}_i}{Dt} = -\frac{1}{m_i} \sum_j (p_i V_i^2 + p_j V_j^2) \nabla_i W_{ij} + \frac{1}{m_i} \sum_j \frac{2\mu_i \mu_j}{\mu_i + \mu_j} (V_i^2 + V_j^2) \times \frac{\mathbf{r}_{ij} \cdot \nabla_i W_{ij} \mathbf{u}_{ij}}{r_{ij}^2} + \mathbf{g}_i \quad (16)$$

Considering that the same particle volume is used for different fluid phases in this work, $V_i = V_j$, Eq. (16) can be simplified as:

$$\frac{D\mathbf{u}_i}{dt} = -\frac{1}{\rho_i} \sum_j (p_i + p_j) V_j \nabla_i W_{ij} + \frac{1}{\rho_i} \sum_j \frac{4\mu_i \mu_j}{\mu_i + \mu_j} \frac{\mathbf{r}_{ij} \cdot \nabla_i W_{ij}}{r_{ij}^2} V_j \mathbf{u}_{ij} + \mathbf{g}_i \quad (17)$$

In the WCPH method, the thermodynamic pressure p is calculated explicitly by the Tait equation of state [17], for particle i is given by:

$$\rho_i = B_i \left(\left(\frac{\rho_i}{\rho_{0i}} \right)^\gamma - 1 \right), \quad B_i = \frac{\rho_i c_0^2}{\gamma} \quad (18)$$

where the coefficient γ is a constant taken equal to 0.1, and c_0 is a numerical sound velocity under the reference density. Generally, the

c_0 is greater than ten times the maximum flow velocity to ensure the density fluctuation is within 1%. At the same time, the selected c_0 is much less than the actual sound velocity to avoid very small time steps. Usually c_0 is limited by the following equations [75]:

$$c_0 \geq 10 \max \left(\sqrt{\frac{p_{\max}}{\rho_0}}, u_{\max} \right) \quad (19)$$

where, p_{\max} and u_{\max} are the maximum expected pressure and expected velocity in the flow field.

In the viscosity formula, the effective viscosity $\mu = \mu_t + \mu_{f/s}$ is the sum of the turbulent viscosity and the physical viscosity of the fluid. The physical viscosity of water is $\mu_f = 10^{-3} \text{ Pa} \cdot \text{s}$, the physical viscosity of sediment particles μ_s is given by the rheological model. The turbulence viscosity is calculated by the large eddy simulation sub-particle-scale turbulence closure model. The turbulent viscosity formula proposed by Di Mascio et al. [76] is adopted in this work:

$$\mu_{ti} = \rho_i (C_s l_{LES})^2 \|\mathbf{D}\|_i \quad (20)$$

where $C_s = 0.12$ is the Smagorinsky constant, l_{LES} is the reference length of the SPH filtering process, it is set to be equal to the radius of the core (i.e., $l_{LES} = 2h = 4\Delta x$). $\|\mathbf{D}\|$ is as follows:

$$\|\mathbf{D}\| = \sqrt{2\mathbf{D} : \mathbf{D}} \quad (21)$$

Among them, the strain rate tensor is calculated using the following formula:

$$\mathbf{D} = \frac{1}{2} \sum_j [(\mathbf{u}_j - \mathbf{u}_i) \otimes (\mathbf{L}_i \cdot \nabla W_{ij}) + (\mathbf{L}_i \cdot \nabla W_{ij}) \otimes (\mathbf{u}_j - \mathbf{u}_i)] V_j \quad (22)$$

where \mathbf{L}_i is a renormalization matrix:

$$\mathbf{L}_i = [\sum_j (\mathbf{r}_j - \mathbf{r}_i) \otimes \nabla_i W_{ij} V_j]^{-1} \quad (23)$$

2.4. $\mu(I)$ rheological model

The effective viscosity η of granular materials is determined by the rheological model, and its expression relies on the material studied. The rheological model selected in the present work is a frictional model based on $\mu(I)$ law [37]. This model is obtained based on most experiments and numerical simulations and provides a general framework to describe the behavior of various granular materials [48]. The effective viscosity η of the $\mu(I)$ rheological model is given by:

$$\eta = \frac{\mu(I)p_s}{2\|\mathbf{E}\|} \quad (24)$$

where p_s denotes the inter-grain mechanical pressure, the $\mu(I)$ indicates the inertial-dependent friction coefficient, the value is determined by the inertial number I and is given as follows:

$$\mu(I) = \mu_1 + \frac{\mu_2 - \mu_1}{I_0/I + 1} \quad (25)$$

in which μ_1, μ_2 denote the first and second friction coefficients, which are the higher and lower limits of the friction coefficient $\mu(I)$, respectively. I_0 represents the reference inertial number, generally derived from the experiment. Therefore, the effective viscosity η can be rewritten as:

$$\eta = \frac{\mu_1 p_s}{2\|\mathbf{E}\|} + \frac{\mu_2 - \mu_1}{I_0/I + 1} \frac{p_s}{2\|\mathbf{E}\|} \quad (26)$$

The inertial number I is defined as the ratio of the microscopic and the macroscopic timescales and depends on the regime of granular

flows [8,77]. It is given by $I = \|\mathbf{E}\|d_s/\sqrt{p_s/\rho_g}$ for free fall regime (dry regime), $I = \|\mathbf{E}\|d_s/\sqrt{p_s/(\rho_f c_d)}$ for the inertial regime (submerged/saturated regime, in which the Stokes number $s_t = \frac{d_s \sqrt{\rho_f p_s}}{\eta_f} \gg 1$), where d_s denotes the granular diameter and c_d denotes the drag coefficient equal to 0.4 [78,79]. η_f and ρ_f denote the viscosity and density of the ambient fluid, respectively. Substituting the inertial number into Eq. (26), and the exponential regularization form proposed by Papanastasiou [80] is applied. The final form of effective viscosity η for two granular regimes is as follows:

$$\eta = \begin{cases} \frac{\mu_1 p_s (1 - \exp(-m\|\mathbf{E}\|))}{2\|\mathbf{E}\|} + \frac{(\mu_2 - \mu_1)d_s \sqrt{\rho_g}}{I_0 + \|\mathbf{E}\|d_s/\sqrt{p_s/\rho_g}} \frac{\sqrt{p_s}}{2} & \text{Dry regime} \\ \frac{\mu_1 p_s (1 - \exp(-m\|\mathbf{E}\|))}{2\|\mathbf{E}\|} + \frac{(\mu_2 - \mu_1)d_s \sqrt{\rho_f c_d}}{I_0 + \|\mathbf{E}\|d_s/\sqrt{p_s/(\rho_f c_d)}} \frac{\sqrt{p_s}}{2} & \text{Submerged regime} \end{cases} \quad (27)$$

where m represents an index that controls the viscosity growth. The effective viscosity of the granular materials reaches the finite maximum value for $\|\mathbf{E}\| \rightarrow 0$.

Additionally, it is necessary to calculate the mechanical pressure p_s between grains. When the granular materials are in a dry regime, the mechanical pressure is equivalent to the thermodynamic pressure: $p_s = p$. But the WCSPH method will cause some non-physical pressure fluctuations, which can affect the behavior of the granular materials pre- and post-failure [1]. To minimize the influence of pressure fluctuations as much as possible, the Shepard filter is used here:

$$\langle p \rangle_i = \frac{\sum_j p_j W_{ij} V_j}{\sum_j W_{ij} V_j} \quad (28)$$

2.5. Dynamic effective pressure methodology

As for effective pressure, herein, referring to Jandaghian et al. [38], we adopted the consistent dynamic method to estimate the effective pressure, which is based on the mass conservation of pore water (in the mixture phase). The accuracy of the consistent effective pressure method has been verified by Jandaghian et al. [38]. To this end, we apply the main assumptions that have been considered in the model based on the single-phase continuum of a completely submerged granular flow. The continuity equation controlling the density of the pore water part $\bar{\rho}_{pw} = (1-\phi)\rho_w$ is given as:

$$\frac{1}{\bar{\rho}_{pw}} \frac{D^w \bar{\rho}_{pw}}{Dt} + \frac{1}{V_M} \frac{D^w V_M}{Dt} = 0 \quad (29)$$

where $D^w(\cdot)/Dt$ denotes the material derivative of the fluid phase [81]. ρ_w is the true water density of the mixture phase of pore water pressure (as a positive pressure fluid) [43]. Since the single-phase model treats the mixture of particles and pore water as a single continuum, the fluid flow in the solid framework is ignored [38]. Therefore, it is assumed that the volume fraction remains constant (that is, $\phi = \text{constant}$), and the position and velocity of the pore water phase and the mixture phase are the same (that is, $V_{pw} = V$ and $D^w(\cdot)/Dt = D(\cdot)/Dt$. Therefore, the general form of the constitutive relationship of the pore water pressure in the submerged particle phase can be expressed as follows:

$$\begin{cases} \frac{1}{\rho_w} \frac{D\rho_w}{Dt} + \frac{1}{V_M} \frac{DV_M}{Dt} = 0 \\ p_{pw} = f(\rho_w) \end{cases} \quad (30)$$

Finally, the effective pressure is determined by the effective stress of Terzaghi and the equation of state of the mixture and the pore water phase, expressed as $p_{eff} = p - p_{pw}$.

2.6. Particle shifting technique (PST)

The particle shifting technique (PST) can redistribute particles in a more isotropic manner, avoiding the dispersion error of particle aggregation in the compression direction and sparse dispersion error in the stretching direction [82]. The PST was first put forward by Xu et al. [83] based on the ISPH method; however, this method cannot be used directly for free surface flow problems. The improved PST presented by Lind et al. [84] describes an effective method to deal with the shifting of particles on and near the free surface. Khayyer et al. [85] presented an optimized particle shifting scheme to achieve accurate and consistent shifting of particles in free surface flow problems. Sun et al. [55] proposed a modified PST in the context of WCSPH, which considers the influence of Mach number and is suitable for the multi-resolution issue. The idea of these improved PSTs is to deal with the free surface and its neighboring particles by removing the shifting along the normal direction. However, for the long-term free surface flow problems, this method may lead to the non-physical gap between the free surface and internal particles. Wang et al. [86] proposed an improved particle shifting technology (IPST) based on Sun et al. [55] to provide more accurate particles shifting in the vicinity region of the free surface. The main idea is that for internal particles, the shifting vectors are the same as that of Sun et al. [55]. The free surface particles will not be shifted to avoid non-physical motion. For particles near the free surface, their shifting vectors are similar to that of internal fluid particles, but with smaller shifting distances.

In this work, the IPST is extended to the multi-phase granular flows. For the two-phase granular flows, the particles shifting process consists of a two-step. First, the IPST is performed only for the granular phase while the fluid phase is ignored. Since the ambient fluid is ignored, the surface of the granular phase will be recognized as the free surface. Then, the IPST is performed for the fluid phase while the granular phase is also considered. The fluid-type particles on the phase interface hence are identified as inner particles. The described two-step shifting procedure guarantees that the two-phase particles will not penetrate each other artificially; it can also ensure the almost perfect regularized particle distribution in this domain [87]. The particle shifting vector of multi-phase granular flows is expressed as follows:

$$\delta\mathbf{r}_i = \begin{cases} 0 & \text{if } i \in F_r \\ -0.5U_{max} \cdot h \cdot \Delta t \sum_j 0.24 \left(\frac{W_{ij}}{W(\Delta x)} \right)^4 \nabla_i W_{ij} V_j, j \in [|r_{ij}| < l_i] & \text{if } i \in V_r \\ -0.5U_{max} \cdot h \cdot \Delta t \sum_j \left[1 + 0.24 \left(\frac{W_{ij}}{W(\Delta x)} \right)^4 \right] \nabla_i W_{ij} V_j, j \in [|r_{ij}| < 2h] & \text{if } i \in I_r \end{cases} \quad (31)$$

where F_r , V_r , I_r represent the free surface, free surface vicinity region, and internal fluid region, respectively. l_i denotes the distance between the particle i and its nearest free surface particle.

2.7. Time-stepping scheme

In summary, the WCSPH discrete form of the multi-phase granular flows control equation (system (1)) is as follows:

$$\begin{cases} \frac{d\rho_i}{dt} = -\rho_i \sum_j (\mathbf{u}_j - \mathbf{u}_i) \cdot \nabla_i W_{ij} V_j + D^{\delta+MSPH} \\ \frac{du_i}{dt} = -\frac{1}{\rho_i} \sum_j (p_i + p_j) \nabla_i W_{ij} V_j + \frac{1}{\rho_i} (\eta \nabla^2 \mathbf{u})_i + \mathbf{g} \\ \frac{d\mathbf{r}_i}{dt} = \mathbf{u}_i, \mathbf{r}_i^* = \mathbf{r}_i + \delta\mathbf{r}_i, p_i = B_i \left(\left(\frac{\rho_i}{\rho_{0i}} \right)^\gamma - 1 \right) \end{cases} \quad (32)$$

where the incremental diffusive term D_i^δ , viscosity term $\eta \nabla^2 \mathbf{u}$ and the shifting vector formula $\delta\mathbf{r}_i$ are discussed in Section 2.3.1, Section 2.4.1, and Section 2.5, respectively.

The system (32) is solved by a 4th-order Runge–Kutta integration algorithm adopting a frozen diffusive method [88]. Based on several criteria, the time integration step Δt is limited by stability [89]. The following three conditions are the CFL conditions according to artificial sound speed:

$$\nabla t \leq \text{CFL} \frac{h}{c_0} \quad (33)$$

viscosity condition:

$$\nabla t \leq 0.125 \frac{h^2}{\max(v_i)} \quad (34)$$

and the force condition:

$$\nabla t \leq 0.25 \min \sqrt{\frac{h}{|f_i|}} \quad (35)$$

where CFL is the Courant–Friedrichs–Lowy constant set to 1.25, v_i denotes the coefficient of kinematic viscosity of fluid or granular phase, f_i is the force per unit mass. The minimum of the three conditions is used as the final time step.

3. Boundary conditions

3.1. Solid boundary conditions

The robustness and accuracy of simulation results largely depend on the boundary implementation technology in the SPH method. In all cases of this paper, the solid boundary is implemented by the fixed ghost particle method proposed by Marrone et al. [66] and Adami et al. [90]. The physical quantities of ghost particles are interpolated directly from the flow field, and the expression of the ghost particle pressure is as follows:

$$p_s = \frac{\sum_f p_f W_{sf} + (\mathbf{g} - \mathbf{a}_s) \sum_f \rho_f \mathbf{r}_{sf} W_{sf}}{\sum_f W_{sf}} \quad (36)$$

in which “s” denotes the ghost particle, “f” denotes the fluid particle, \mathbf{a}_s denotes the acceleration of the ghost particle.

3.2. Friction boundary conditions

In the numerical simulation of granular flow, the influence of foundation friction is mostly ignored. However, previous studies [61,62] have shown that the impact of foundation friction on granular flow results is very significant. In this work, friction boundary conditions of the momentum method proposed in Sheikh et al. [60] are used to mimic the interaction between the granular material and the solid boundary to consider the influence of ramp friction on the evolution of granular landslides.

The schematic of the momentum method is shown in Fig. 2. The procedure is based on the momentum exchange between the boundary surface and the sediment particles [60]. First, based on the assumption of a completely elastic collision, the relative velocity $\Delta\mathbf{u}_i$ between the sediment particle i and the boundary when a collision occurs can be calculated as $\Delta\mathbf{u}_i = \mathbf{u}_b - \mathbf{u}_i$. According to $\Delta\mathbf{u}_i$ and the mass of particle i , the formula for calculating the component of the boundary reaction force \mathbf{F}_i can be obtained from the momentum theorem, as follows:

$$\mathbf{F}_i^n = \frac{2m_i \Delta\mathbf{u}_i^n}{\Delta t}, \mathbf{F}_i^T = \frac{2m_i \Delta\mathbf{u}_i^T}{\Delta t} \quad (37)$$

where $\Delta\mathbf{u}_i^n = (\Delta\mathbf{u}_i \cdot \mathbf{n}) \mathbf{n}$ and $\Delta\mathbf{u}_i^T = \Delta\mathbf{u}_i - \Delta\mathbf{u}_i^n$ are the normal and tangential components of $\Delta\mathbf{u}_i$, respectively. There is no energy loss since Eq. (37) is based on a completely elastic collision. In order to

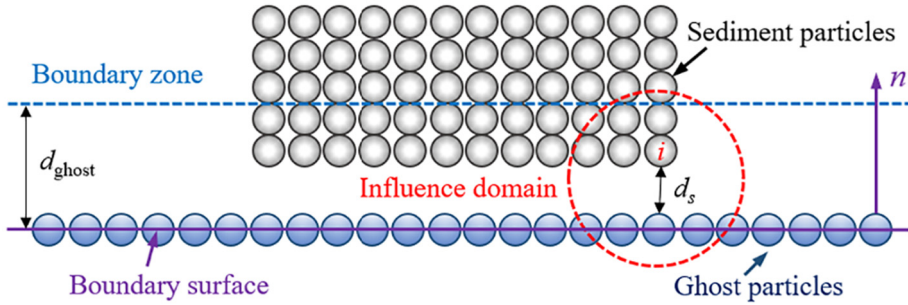


Fig. 2. Schematic diagram of the momentum method.

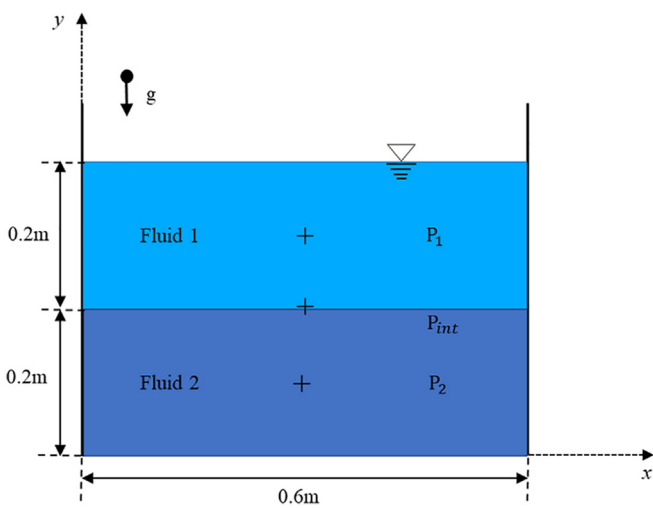


Fig. 3. Geometrical details of the numerical tank and location of pressure measurement points.

include controllable energy loss during contact, the normal component of velocity can be modified as $\Delta\mathbf{u}_i^n = \beta'(1-D)\Delta\mathbf{u}_i^n$, and the energy loss is determined by D . With regard to frictional contact, the tangential component of velocity can be modified to:

$$\Delta\mathbf{u}_i^{\tau'} = \begin{cases} \mu \frac{|\mathbf{F}_n|}{|\mathbf{F}_{\tau}|} \Delta\mathbf{u}_i^{\tau}, & \text{if } |\mathbf{F}_i^{\tau}| > \mu |\mathbf{F}_i^n| \\ \Delta\mathbf{u}_i^{\tau}, & \text{otherwise} \end{cases} \quad (38)$$

If particle *i* enters the boundary region (controlled by d_{ghost}), the boundary reaction force should be added to the momentum equation ($\mathbf{u}_i \cdot \mathbf{n} < 0$) only when the particle moves to the boundary surface [60]. Therefore:

$$\mathbf{F}_i^n = \frac{2m_i\beta'(1-D)\Delta\mathbf{u}_i^n}{\Delta t}, \mathbf{F}_i^{\tau} = \frac{2m_i\Delta\mathbf{u}_i^{\tau'}}{\Delta t} \quad (39)$$

$$\mathbf{F}_i = \begin{cases} \left\{ \begin{array}{ll} \mathbf{F}_i^n + \mathbf{F}_i^{\tau} & \Delta d_p^n > 0 \\ 0 & \text{otherwise} \end{array} \right. & \mathbf{u}_i \cdot \mathbf{n} < 0 \\ 0 & \text{otherwise} \end{cases} \quad (40)$$

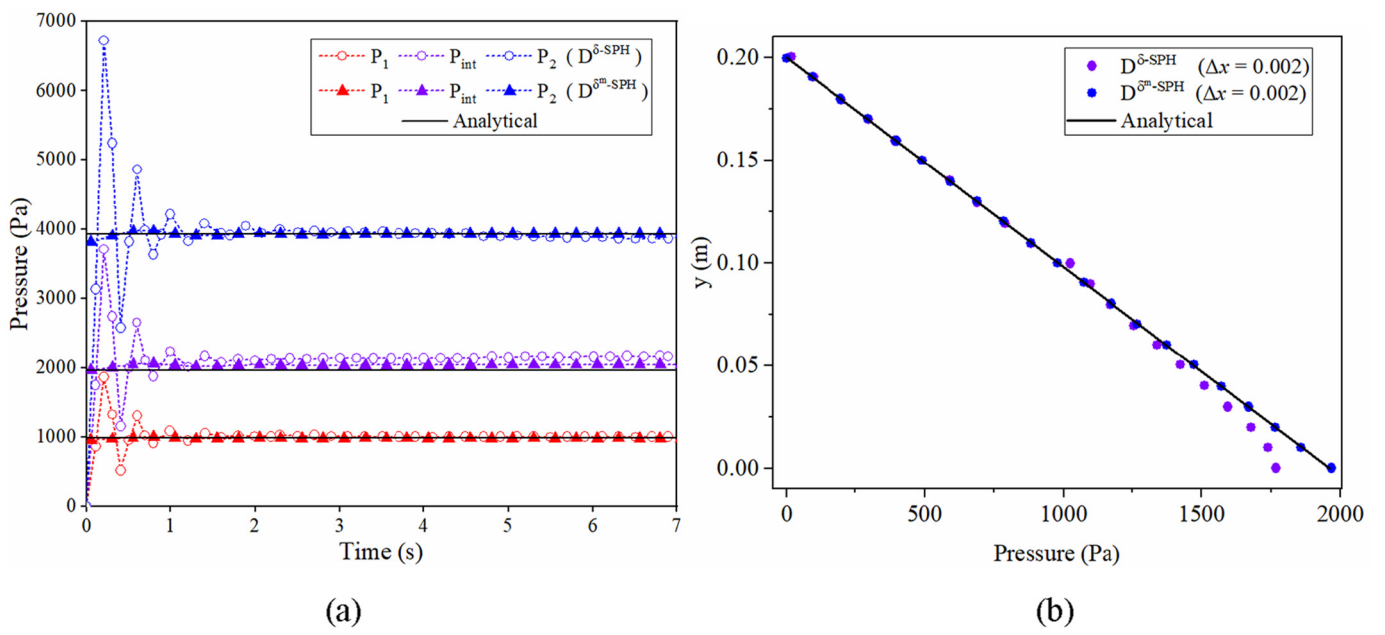


Fig. 4. (a) The pressures history of three measurement points P_1 , P_{int} and P_2 ; (b) The position of the fluid particle versus its numerical pressure when $t = 10.0$ s. The results are compared with the traditional diffusive term $D^{\delta\text{-SPH}}$ and the analytical value.

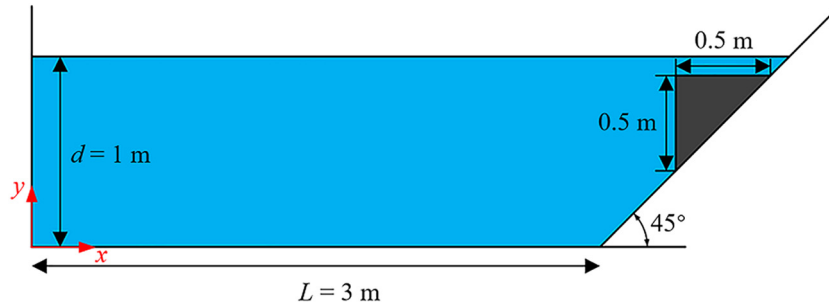


Fig. 5. Geometric configuration of Heinrich [96] experiment.

where $\beta' = d_{\text{ghost}}/d_s$, $\Delta d_p^{\text{in}} = d_{\text{ghost}} - d_s$, $d_{\text{ghost}} = h$ is the thickness of the boundary zone, which remains unchanged in the simulation, d_s denotes the vertical distance between the particle and the boundary surface.

4. Applications

4.1. Hydrostatic pressure of two-phase stratified fluids

This benchmark case is mainly to prove that the proposed incremental diffusive term ($D^{\delta m-\text{SPH}}$) has robust performance in reducing and smoothing the pressure oscillation in the multi-phase WCSPH model. The results are compared with the data calculated by the traditional diffusive term $D^{\delta-\text{SPH}}$. As Fig. 3 shows, a 2D numerical tank with a length of 0.6 m and a height of 0.45 m is used in this work [31]. The fluid in the tank is arranged in layers. The upper fluid (named fluid 1) is lighter, with a density of $\rho_1 = 1000 \text{ kg/m}^3$ and the lower fluid (named fluid 2) has a density of $\rho_2 = 2000 \text{ kg/m}^3$. The fluids in the upper and lower layers are both Newtonian fluids, and their viscosities are: $\mu_1 = 0.02 \text{ Pa} \cdot \text{s}$ and $\mu_2 = 0.001 \text{ Pa} \cdot \text{s}$, respectively. The particle initial spacing is of $\Delta x = 0.01 \text{ m}$, resulting in 2988 total particles. Three pressure measurement points P_1 (0.3, 0.5), P_{int} (0.3, 0.2), and P_2 (0.3, 0.1) are arranged in the numerical tank to record the change of pressure value in the process of numerical simulation, which is located in the layer center of fluid 1, the interface of two fluids and the layer center of fluid 2.

Fig. 4(a) shows the pressures change versus time of three measurement points P_1 , P_{int} and P_2 . The results of the proposed incremental diffusive term $D^{\delta m-\text{SPH}}$ are compared with the results calculated by the traditional diffusive term $D^{\delta-\text{SPH}}$ and the analytical hydrostatic pressure values. It is observed that when the incremental diffusive term $D^{\delta m-\text{SPH}}$ is used, the computed pressure at different measurement points is steady to the hydrostatic pressure value after $t = 1 \text{ s}$. In contrast, the calculated pressure of the traditional diffusive term is steady only after $t = 2.5 \text{ s}$ and presents an obvious error, especially at the phase interface. Fig. 4(b) shows the position of the fluid particle versus its numerical pressure when $t = 10 \text{ s}$. The results indicate that the traditional diffusive term causes the divergence of the pressure field near the bottom wall. The nuclear truncation in these regions affects the particle number density field, resulting in the instability of the pressure field in the long-term simulation of the research problem. By using the incremental diffusive term form, the numerical pressures at the interface and the bottom wall are consistent with the analytical results. The incremental diffusive term can solve the problem of nuclear truncation near the free surface and the wall.

4.2. Rigid landslides

Thanks to the frictional boundary conditions that can mimic the interaction between rigid landslides and the slope, the numerical model proposed in this work is also suitable for solving the motion of the rigid landslide on the slope by introducing the rigid body motion

equation [67]. The model in this work does not need to pre-specify the movement of the landslide based on experimental data compared with the traditional SPH rigid landslide model [32,91,92]. Compared with some recently developed methods for solving rigid landslide motion [93–95], the proposed method can not only consider the influence of dynamic friction but also does not require introducing additional numerical methods (such as DEM).

The physical test of submarine landslide-tsunami in [96] is numerically simulated in this section. As shown in Fig. 5, the rigid landslide is a triangular wedge with a length and width of 0.5 m and a density of 2000 kg/m^3 . The still water depth is 1 m, and the landslide is initially placed 0.01 m below the free water surface. In the SPH numerical model, the particle spacing is $\Delta x = 0.01 \text{ m}$, a total of 36,658 particles are produced, and the wall friction coefficient $\mu = 0.045$.

Fig. 6 presents the comparison of the landslide's vertical displacement time history obtained in this article with the experimental data [96] and the numerical results obtained by the DNS method [97] and the ISPH method [94]. These three numerical methods show good agreement with the experimental data. However, the landslide velocity is overestimated after $t = 0.8 \text{ s}$ due to the ignored friction effect in ISPH [94] and DNS [97] models. Since the dynamic friction is considered in the current study, the displacement of the rigid landslide is closer to the experimental results.

As Fig. 7 illustrates, the calculated results of free surface wave profiles at typical times (a) $t = 0.5 \text{ s}$ and (b) $t = 1.0 \text{ s}$ are compared with Heinrich's experimental data. The results obtained by this article are consistent with experimental data. Some small gaps appear in the upper area of the landslide, which may be caused by the reflected wave on the ramp [98]. The comparison results indicate that the

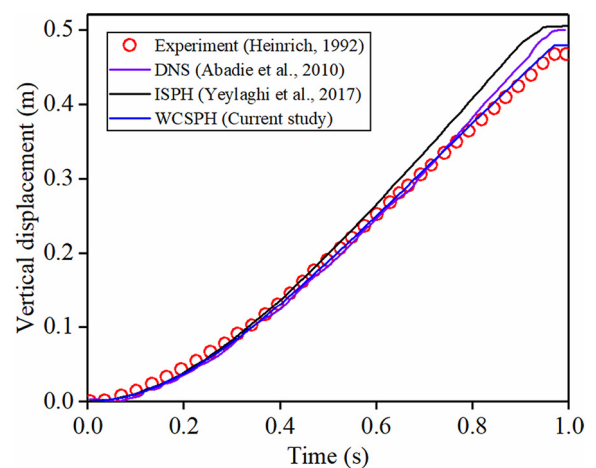


Fig. 6. Comparison of the vertical displacement of the landslide over time obtained by the model in this work with the experiment data and previous numerical results.

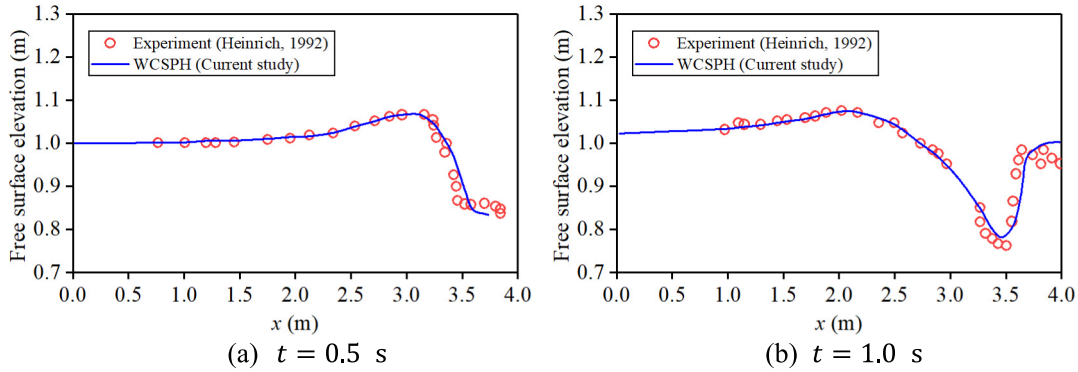


Fig. 7. Comparison of the free surface elevation obtained by the current program with experimental data at (a) $t = 0.5$ s and (b) $t = 1.0$ s.

proposed method is suitable for simulating a non-deformable landslide and does not need to pre-define the motion trajectory of the landslide, which has substantial practical value.

Fig. 8 shows the snapshots of the values obtained by the current WCSPH method, where the particles are colored with their pressure. As described by Yeylaghi et al. [94] and Zhang et al. [98], the movement of the landslide in the water generates two waves. The first wave is produced while the landslide continuously squeezes the water body (Fig. 7(a)–(d)) [98]. Then the second wave is produced by the subduction wave on the slope (Fig. 7(e)–(f)). It is worth noting that at $t = 0.97$ s, the landslide is forced to stop moving. Due to inertia, the water above the landslide impacts the landslide, causing a large pressure field in this area, while the water on the left of the landslide is far away from the landslide. This results in a vacuum (negative pressure) in this area (Fig. 7(d)). Subsequently, the pressure shock spreads to the entire computational domain and gradually decays. At $t = 2.5$ s, the pressure field has stabilized (Fig. 7(f)).

4.3. Dry granular landslides

According to the types of interstitial and ambient fluids, the granular landslides regimes can be divided into three types [79]. The first type is

dry granular landslides, where the ambient and interstitial fluids are the air, and the movement of the granular materials is dominated by free fall. The second type is submerged landslides, where ambient and interstitial fluids are the water, and the inertial regime of granular materials is dominant. The third type is sub-aerial landslides, which change from dry grains to submerged states as the landslides enter the water.

The dry granular landslides experiment has been conducted by Tajnesaei et al. [8]. The geometrical configuration of their experiment is shown in Fig. 9. An initially triangular pile of granular materials with the length and height of 0.06 m respectively is created behind the gate on the ramp. The granular materials are glass beads with a density of $\rho_g = 2500 \text{ kg/m}^3$ and diameter of $d_s = 0.8 \text{ mm}$. The relevant parameters of $\mu(\text{I})$ rheological model are: $l_0 = 0.279$, $\mu_1 = \tan(20.9^\circ)$, $\mu_2 = \tan(32.76^\circ)$.

The WCSPH model is used to simulate the behavior of dry granular landslides after release. In the current model, the particle resolution is $\Delta x = 0.001 \text{ m}$ (larger than the diameter d_s of glass beads), and a total of 4476 particles are produced. The characteristic time $\sqrt{h_0/g}$ (the free-fall time scale) and the characteristic length h_0 (the initial elevation of granular landslides) are adopted for the normalization of numerical results. Subsequently, the comparison between the results

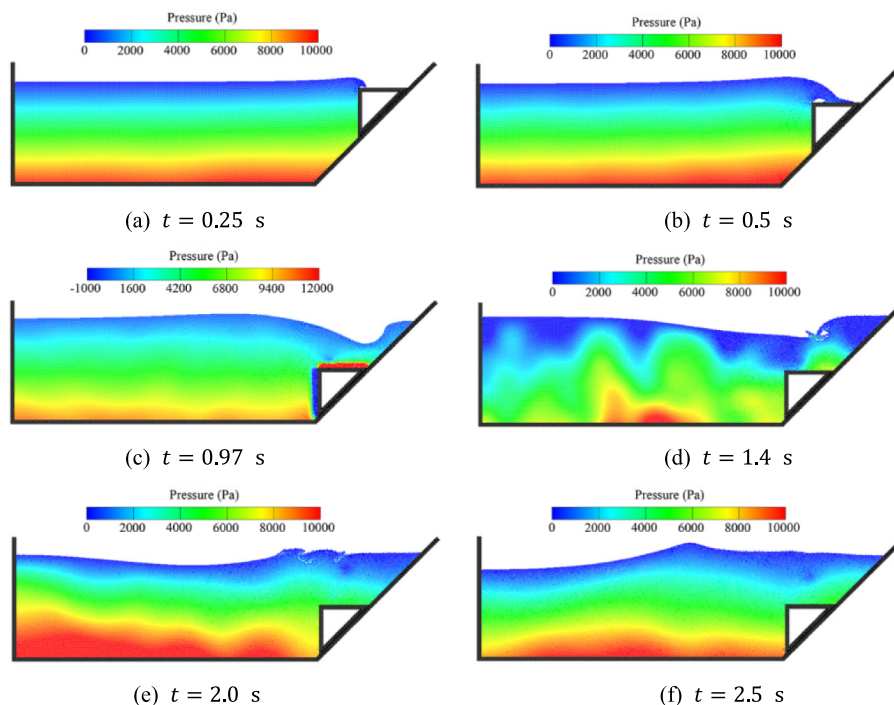


Fig. 8. Snapshots of the results (pressure field) obtained by the current model at typical moments $t = 0.25$ s, $t = 0.5$ s, $t = 0.97$ s, $t = 1.4$ s, $t = 2.0$ s and $t = 2.5$ s.

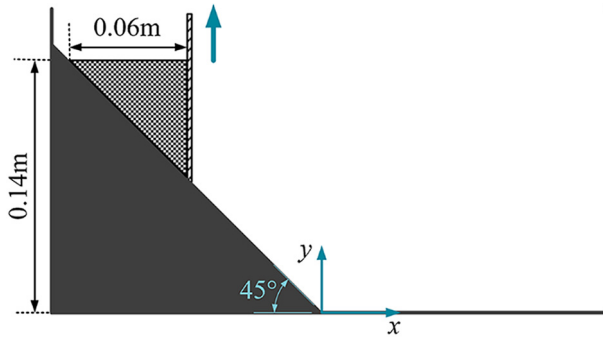


Fig. 9. Geometrical configuration of the sub-aerial granular landslides experiment [8].

of the developed model and experimental data and other numerical results [8] is presented to test the performance of the WCSPH model in dry granular landslide simulation.

Fig. 10 shows the comparison of experimental data [8], WCSPH numerical results (this paper), and MPS numerical results [8] of granular landslides profiles at $[T] = 1$, $[T] = 2$, $[T] = 3$, $[T] = \text{Final}$. $[T] = t/\sqrt{h_0/g}$ denotes the normalized dimensionless time, $[T] = \text{Final}$ represents the time when the granular landslide stops moving. The results show that landslides profiles obtained by two numerical approaches are relatively close and agree with the experimental data. However, the front and tail of numerical landslides obtained by the proposed developments at different times are closer to experimental results.

Fig. 11 shows the comparison of the numerical profiles and experimental snapshots [8] of granular landslides at different dimensionless times ($[T] = 1$, $[T] = 2$, $[T] = 3$, and $[T] = \text{Final}$), where numerical results are colored by the viscosity values of particles. It can be observed in Fig. 11 when the gate was removed, the granular landslide broke from the front and top, forming a high-speed avalanche and flowing down the slope. These failure regions have lower viscosity. As time goes on, the landslides extend along the ramp, impacting the flume bottom and changing its movement direction, resulting in a highly viscous zone at the ramp toe. Then, as the inertial force attenuates and the

viscosity increases [8], the speed of particles in the bottom and center of the landslide slows down, and then extends to the surface and finally stops. Similar phenomena are also reported by Tajnesiae et al. [8] and Pilvar et al. [79]. This indicates that the WCSPH model can describe the behavior of dry granular landslides.

4.4. Submerged granular landslides

In this section, the performance of the WCSPH multi-phase granular flow model is further tested by the numerical simulation of the submarine landslides experiment conducted by Grilli et al. [99]. In their experiment, glass beads with a density of $\rho_g = 2500 \text{ kg/m}^3$ and particle diameter of $d_g = 4 \text{ mm}$ were placed on the slope of 35° under the water and fixed by the gate, and the bulk density is 1892 kg/m^3 . The experimental setup is illustrated in Fig. 12. The length of the tank is 5.75 m and the initial water depth is 0.33 m. Four water level gauges are placed at 0.6 m, 1.6 m, 2.6 m, and 3.6 m away from the gate to record the water surface fluctuation. The experiment starts at $t = 0 \text{ s}$, which corresponds to the withdrawal of the gate into the bottom cavity.

In the WCSPH model, the rheological parameters are: $I_0 = 0.279$, $\mu_1 = \tan(20.9^\circ)$, $\mu_2 = \tan(32.76^\circ)$, following the values reported by Jop et al. [104,105]. These parameters are widely used in the numerical simulation of granular flows [29,36,106]. The wall friction coefficient $\mu = 0.005$. It is worth noting that in the numerical model, the modeling of the gate is related to the particle resolution and the boundary method used, which may have an unrealistic impact on the flow field. Therefore, similar to the previous research [7,31,50], the opening process of the gate is ignored in the numerical simulation.

The particle independence test is conducted and the results of three different resolutions ($\Delta x = 0.002 \text{ m}$, $\Delta x = 0.004 \text{ m}$, and $\Delta x = 0.008 \text{ m}$) are presented in Fig. 13 and Fig. 14. The contours of the pressure field at typical times during the sliding process of the landslide obtained by the SPH procedure are verified with the experimental results of Grilli et al. [99]. Fig. 13 presents the results of $\Delta x = 0.002 \text{ m}$ (left column) and $\Delta x = 0.008 \text{ m}$ (right column). The results of $\Delta x = 0.004 \text{ m}$ are shown in Fig. 14 and are compared with the experimental snapshots. It can be

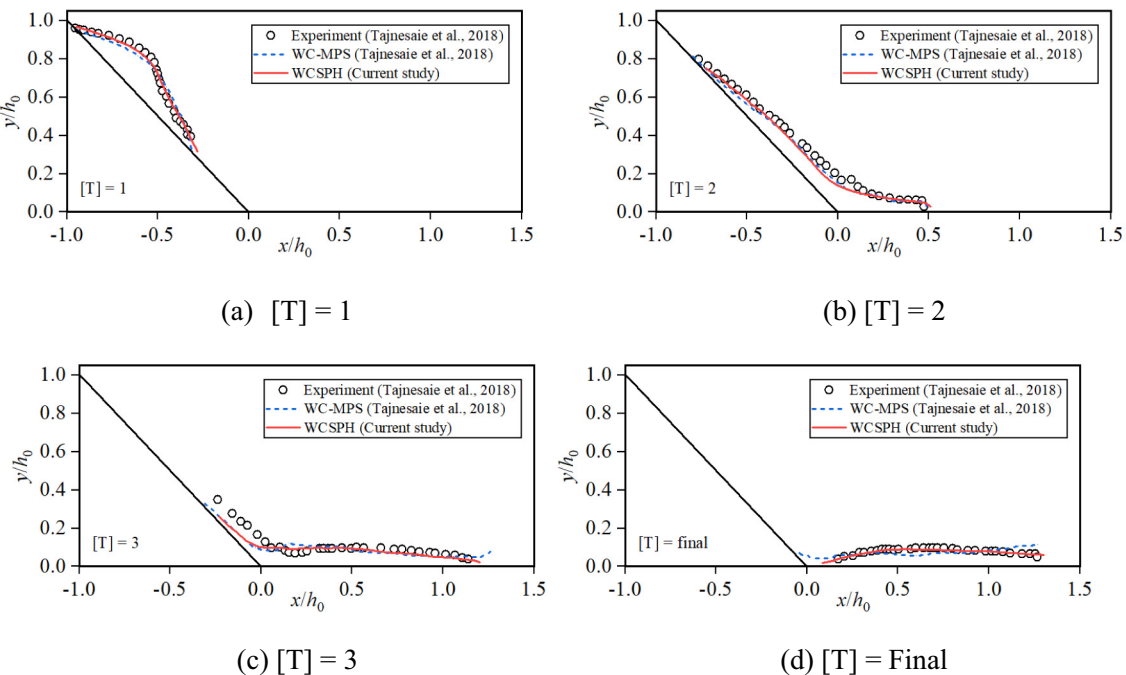


Fig. 10. Landslide profiles at different times, and the results are compared with the experiment data [8] and previous numerical method (MPS).

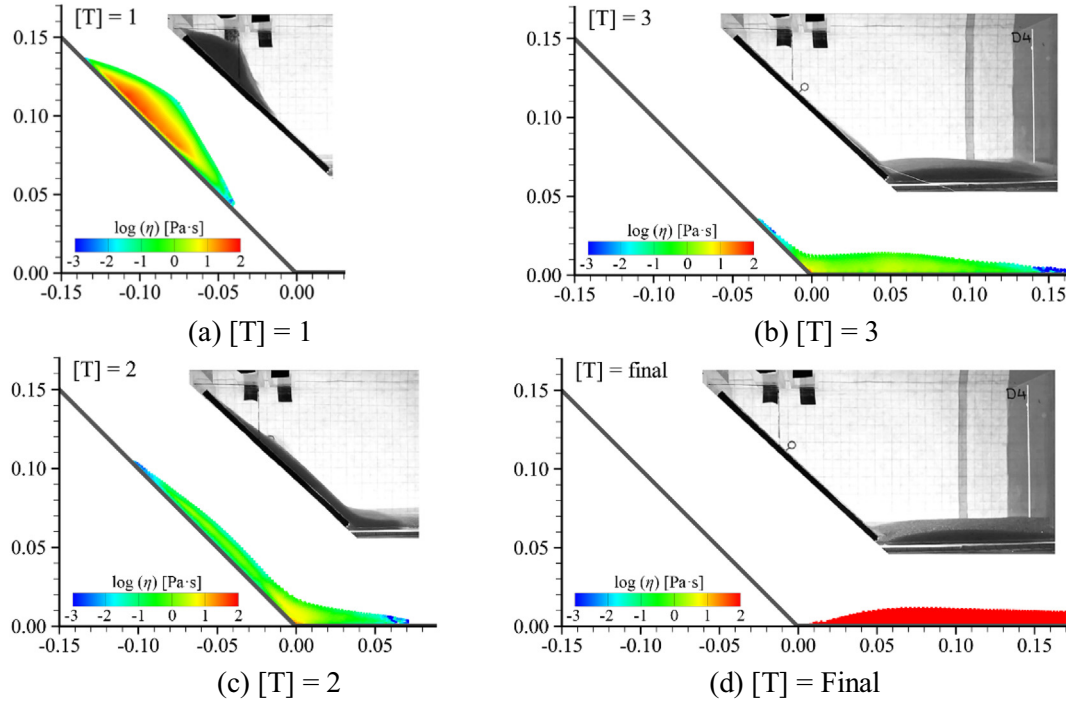


Fig. 11. Comparison of numerical profiles and experimental snapshots [8] of granular landslides, and the numerical results are colored by the viscosities of particles.

seen that there is some gap between the sliding shape of the landslide in the result of $\Delta x = 0.008$ m and the experimental snapshots, indicating that the particle scale used is large. The results of $\Delta x = 0.002$ m and $\Delta x = 0.004$ m can well reflect the experimental phenomenon. When $\Delta x \leq 0.004$ m, the difference between the results is not significant with the increase of particle resolution, which shows that the proposed model is convergent, and the calculation results are independent of the particle scale. In addition, small particle resolution will bring a huge amount of calculation. Therefore, to balance the solution accuracy and calculation efficiency, the results of $\Delta x = 0.004$ m are selected in this section. The computational domain in the model is represented by 118,718 particles. The model is run on a computer with an Intel (R) Core(TM) i7-4790 CPU with 8GB of RAM. It takes 52 h for 10 s of simulation.

Fig. 14 presents the comparison of the calculated landslide section with the experimental snapshots at four moments $t = 0.02$ s, $t = 0.17$ s, $t = 0.47$ s, and $t = 0.62$ s. The fluid particles are colored with the calculated pressure value. It is observed that there is a good consistency between the calculated profile and the measured profile. However, as time marches, the flow front of numerical landslide is slower than the measured value and becomes sharper. Similar reports have been found in Yu et al. [100] and Ghaitanellis [101]. According to the analysis of Ghaitanellis [101], this situation is due to the fact that the

current rheological model can neither represent the flow through granular materials nor the change of particle concentration, which overestimates the pressure resistance and leads to the non-physical reduction of sliding speed. A qualitative comparison with rigid landslides (Fig. 8) shows that due to the fluidity of granular landslides, there will be no sudden changes in the velocity field, leading to a more stable pressure field.

The overall configuration and failure mechanism of submerged granular landslides are similar to the dry granular landslides case [1], but the granular interface is more fluctuating and the front edge of the landslide is thicker. The fluctuations of the particle interface may be related to the viscosity effect of the ambient fluid and ramp slope. The thicker frontier may be associated with the counterclockwise vortex near the landslide front. In addition, it can be observed that some sediments are suspended in the water, which mainly results from the shear stress of ambient fluid. This suspension can also be found in the experiment. Different yielding and non-yielding regions can be identified from the velocity field (Fig. 15) and viscosity field (Fig. 11), but the shape of the interface between these areas is more irregular in the submerged granular landslides case. A surge wave is generated on the surface of the water, while the strength is lower than that of the rigid landslide [8]. It is related to the slight ramp slope of the submerged granular landslides, and the energy dissipation of deformed landslides

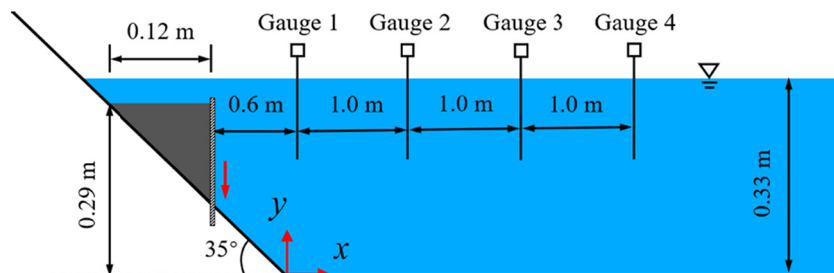


Fig. 12. Geometry of the submerged granular landslides in the experiment of Grilli et al. [99].

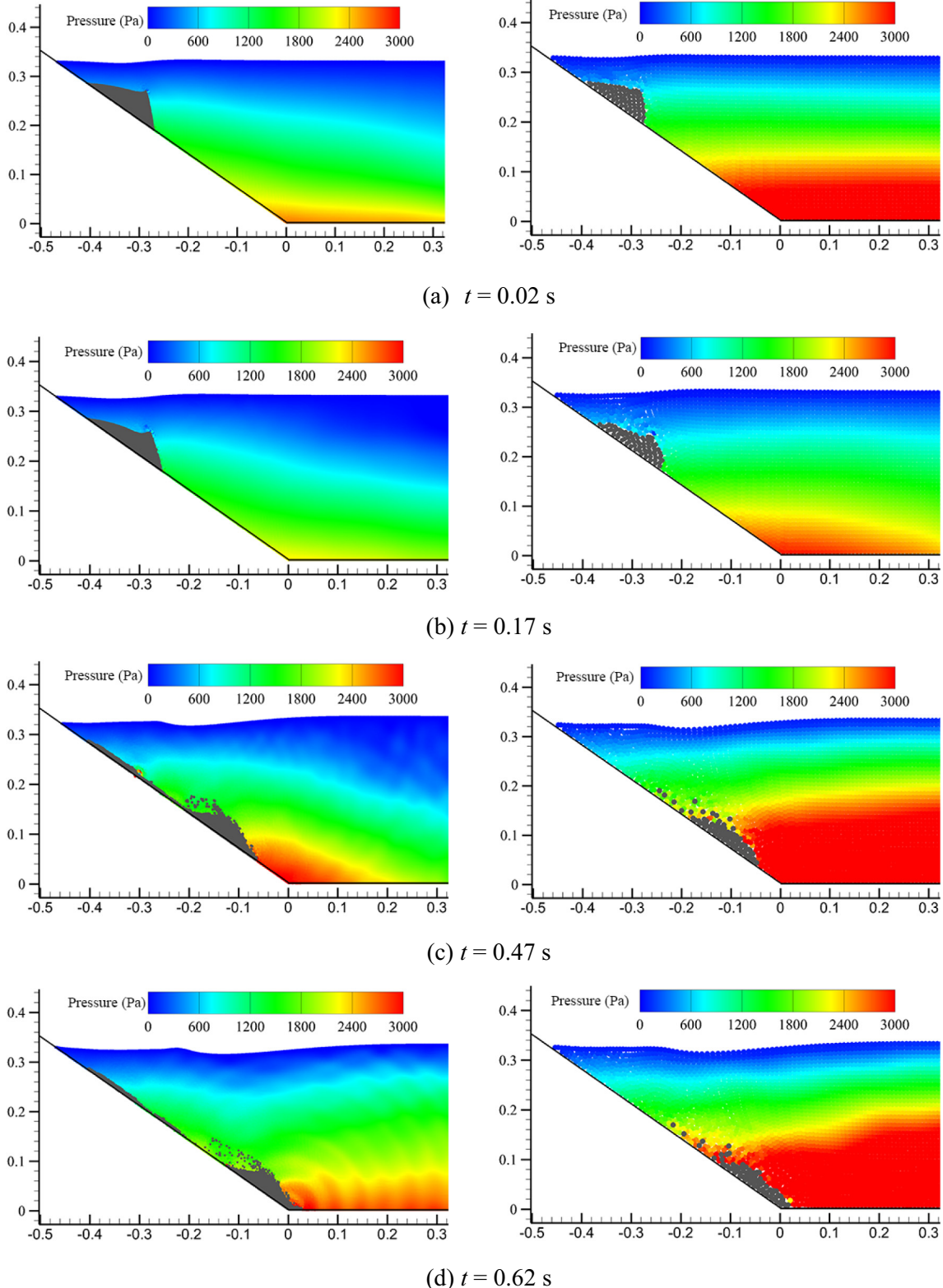


Fig. 13. Granular profiles at typical instants $t = 0.02 \text{ s}$, $t = 0.17 \text{ s}$, $t = 0.47 \text{ s}$, $t = 0.62 \text{ s}$ obtained by the present procedure with particle resolution of $\Delta x = 0.002 \text{ m}$ (left column) and $\Delta x = 0.008 \text{ m}$ (right column).

is greater than that of rigid landslides. This denotes the deformation of the granular has a significant influence on the waves generation by landslides.

Fig. 16 shows the granular profiles of the landslide at (a) $t = 0.02 \text{ s}$, (b) $t = 0.17 \text{ s}$, (c) $t = 0.47 \text{ s}$, (d) $t = 0.62 \text{ s}$, and the results are compared

with those calculated by Grilli et al. [99] using a constant viscosity mesh-based model, and Tajnesiae et al. [8] using VOF model with two viscoplastic rheological models (H–B model and $\mu(I)$ model). The results show that these numerical methods can reflect the experimental phenomena to a certain extent. The results are relatively loose due to

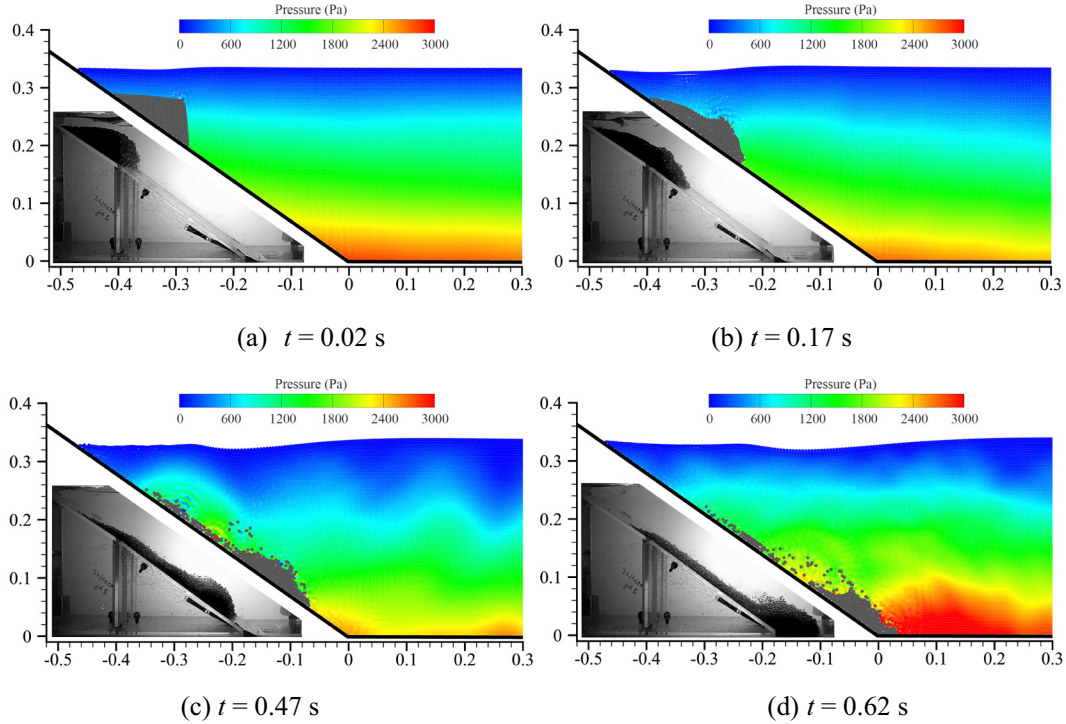


Fig. 14. Comparison of the landslide section calculated by the current model and the experimental snapshots at (a) $t = 0.02$ s, (b) $t = 0.17$ s, (c) $t = 0.47$ s, (d) $t = 0.62$ s, where the fluid particles are colored by the calculated pressure value.

the constant viscosity adopted by Newtonian fluid (Grilli et al. [99]). The results obtained by the present method in this work are relatively close to the experimental data, with a normalized root mean square error (NRMSE) of 0.069 and 0.088 for $t = 0.17$ s and $t = 0.47$ s. The NRMSE for $t = 0.17$ s and $t = 0.47$ s is respectively equal to 0.083, 0.121 for the H-B model [8], 0.073, 0.092 for the $\mu(I)$ model [8], and 0.089, 0.157 for Newtonian model of [99].

4.5. Sub-aerial granular landslides

When the landslide changes from the dry granular state to the submerged state, in addition to the impact of waves, the strong cohesion between partially saturated granular materials has a significant effect on the pre-and post-failure behavior of materials [8]. The proposed model was tested by the sub-aerial granular landslides experiment conducted by Viroulet et al. [102,103]. Their experiments were conducted in a flume with the length, width, and height of 2.2 m, 0.2 m, and 0.4 m, respectively, and the water depth is 0.148 m. The experimental geometry is shown in Fig. 17. The spherical glass beads with a diameter

of $d_s = 1.5$ mm, a mass of 2 kg, and a density of $\rho_g = 2500 \text{ kg/m}^3$ are placed on an inclined surface with a slope of 45° and limited above the free water surface by a vertical gate. The initial profile of the glass beads mass is a triangular shape, and the cross-section is 0.11 m × 0.11 m. Four gauges of water elevation are arranged at 0.45 m, 0.75 m, 1.05 m, and 1.35 m from the gate, respectively. The numerical model has 76,639 particles and the particle's resolution is $\Delta x = 0.002$ m. The parameters of the $\mu(I)$ rheological model are: $I_0 = 0.279$, $\mu_1 = \tan(20.9^\circ)$, $\mu_2 = \tan(32.76^\circ)$. The wall friction coefficient $\mu = 0.005$. The model is run on a computer with an Intel(R) Core(TM) i7-4790 CPU with 8GB of RAM. It takes two days to calculate 5 s of physical time..

Fig. 18 shows the comparison between the numerical and experimental results [102] of granular landslides profiles at: (a) $t = 0.0$ s, (b) $t = 0.1$ s, (c) $t = 0.2$ s, (d) $t = 0.3$ s, (e) $t = 0.4$ s, (f) $t = 0.5$ s. These numerical results include obtained by the proposed method and by Clous and Abadie [107] using the VOF Newtonian fluid and VOF $\mu(I)$ model, respectively. As shown in Fig. 18, for the granular landslides profiles above the water surface, the numerical results are similar to the experimental data. However, for the part that is in the water, the

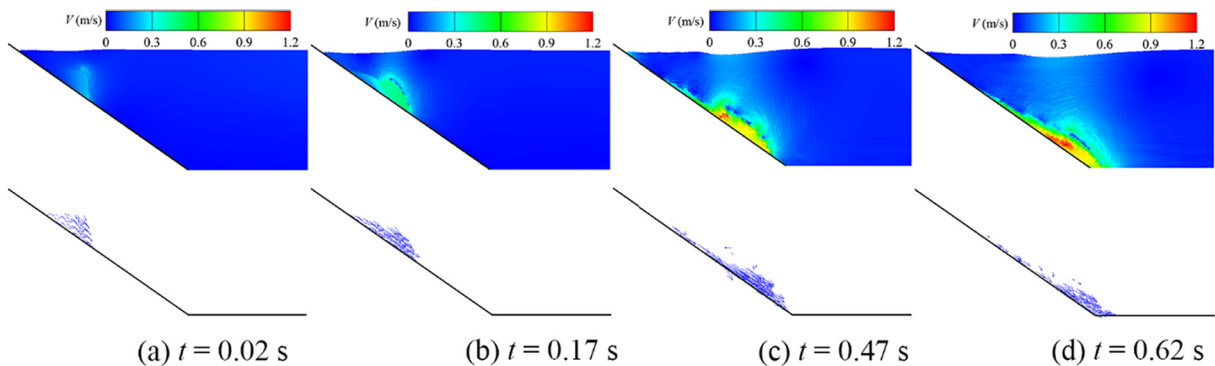


Fig. 15. Numerical velocity and velocity vectors field of submerged granular landslide at: (a) $t = 0.02$ s, (b) $t = 0.17$ s, (c) $t = 0.47$ s, (d) $t = 0.62$ s.

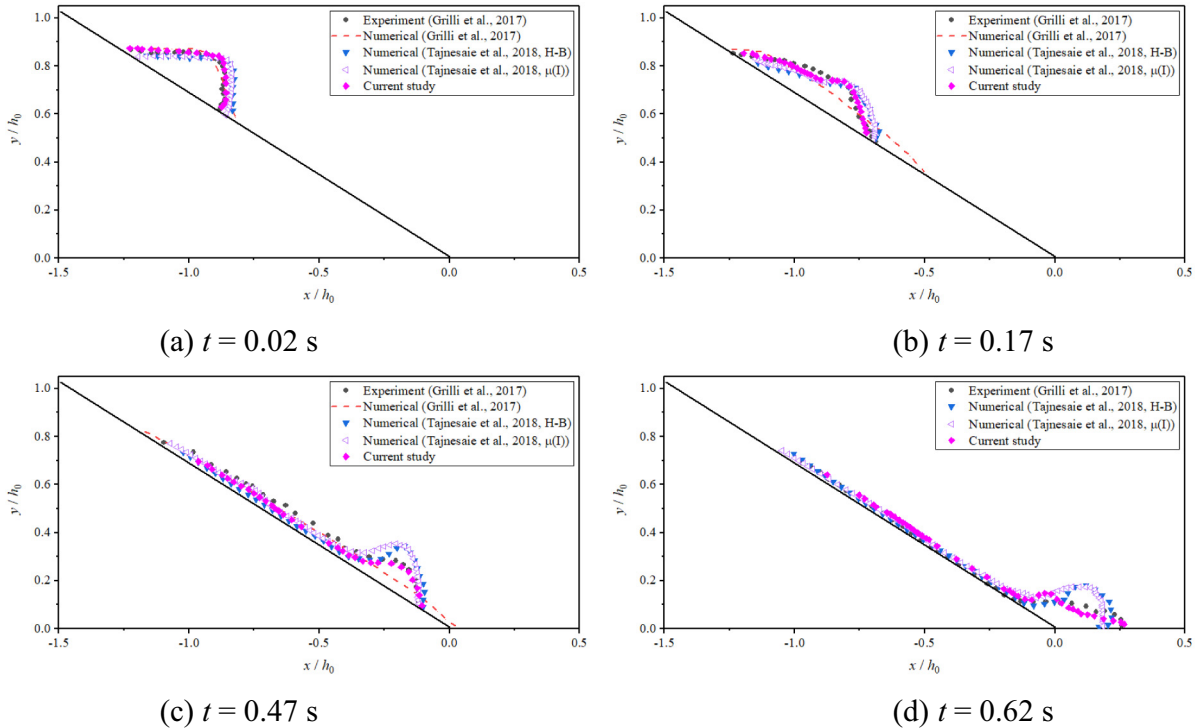


Fig. 16. Granular profiles of the submerged landslide at (a) $t = 0.02$ s, (b) $t = 0.17$ s, (c) $t = 0.47$ s, (d) $t = 0.62$ s, and the results are compared with previous numerical method (Grilli et al. [99] and Tajnesiae et al. [8]).

profiles and positions of granular landslides obtained by the proposed model are closer to the experimental results. The NRMSE for $t = 0.2$ s and $t = 0.5$ s is respectively equal to 0.0168, 0.0228 for the $\mu(I)$ model [107], and 0.0083, 0.0081 for Newtonian fluid [107], and 0.0071, 0.0046 for the proposed model.

The results show that the data obtained by the proposed model are smaller than those in the experiment. This is because in the experiment, when the gate is opened, the fast fluid flow causes the solid particles to suspend in the water, which causes the volume of the mixture to expand [38]. However, the mass exchange between particles is not simulated in the numerical simulation, and the volume expansion observed in the experiment in the beginning stage of landslide is ignored [38]. Therefore, the numerical simulation and experimental curves are not completely consistent.

As Fig. 19 shows, characteristic details of the flow field in the experimental observation are in satisfactory agreement with numerical simulation at (a) $t = 0.21$ s, (b) $t = 0.43$ s, (c) $t = 0.52$ s. The first wave produced by the impact of landslides on the water is shown in Fig. 19 (a); the front part of the elevated water and the fluid region closer to the landslides head have a higher speed. Fig. 19 (b) shows that the velocity around the wave crest has an asymmetric distribution, which

indicates that the impulse wave has not reached a steady state. In Fig. 19 (c), the region in front of the landslide moves upward, while the region behind the wave crest moves downward. These two parts of the fluid meet to form a stagnant zone and move along the flume. A vortex is created in the water region behind the bulge shape landslides, which causes the particles at the top of landslides to roll up, as shown in Fig. 19 (b)-(c). We observe that the roll-up of the landslides head in the numerical simulation is not obvious compared with the experimental observation, which may be caused by the neglect of the mass exchange between the ambient fluid and interstitial fluid in the numerical simulation assumption.

Fig. 20 shows the comparison of numerical results of the free surface elevation versus time with the experimental data [102] at the position: (a) $x = 0.45$ m, (b) $x = 0.75$ m, (c) $x = 1.05$ m, (d) $x = 1.35$ m, and compare with past numerical methods (Clous and Abadie [107]). It can be seen that the results of the proposed multi-phase WSPH model are rather close to experimental results compared with past numerical methods. However, the amplitude of the first wave in the numerical simulation is slightly larger than the experimental data. The reason may be that the numerical method underestimated the exchange of interstitial and ambient fluids, resulting in the excessive impact force on

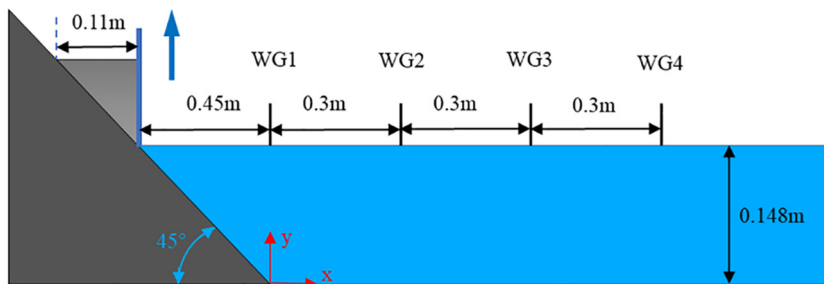


Fig. 17. Sketch of sub-aerial landslides in the experiment and the position of water elevation gauges.

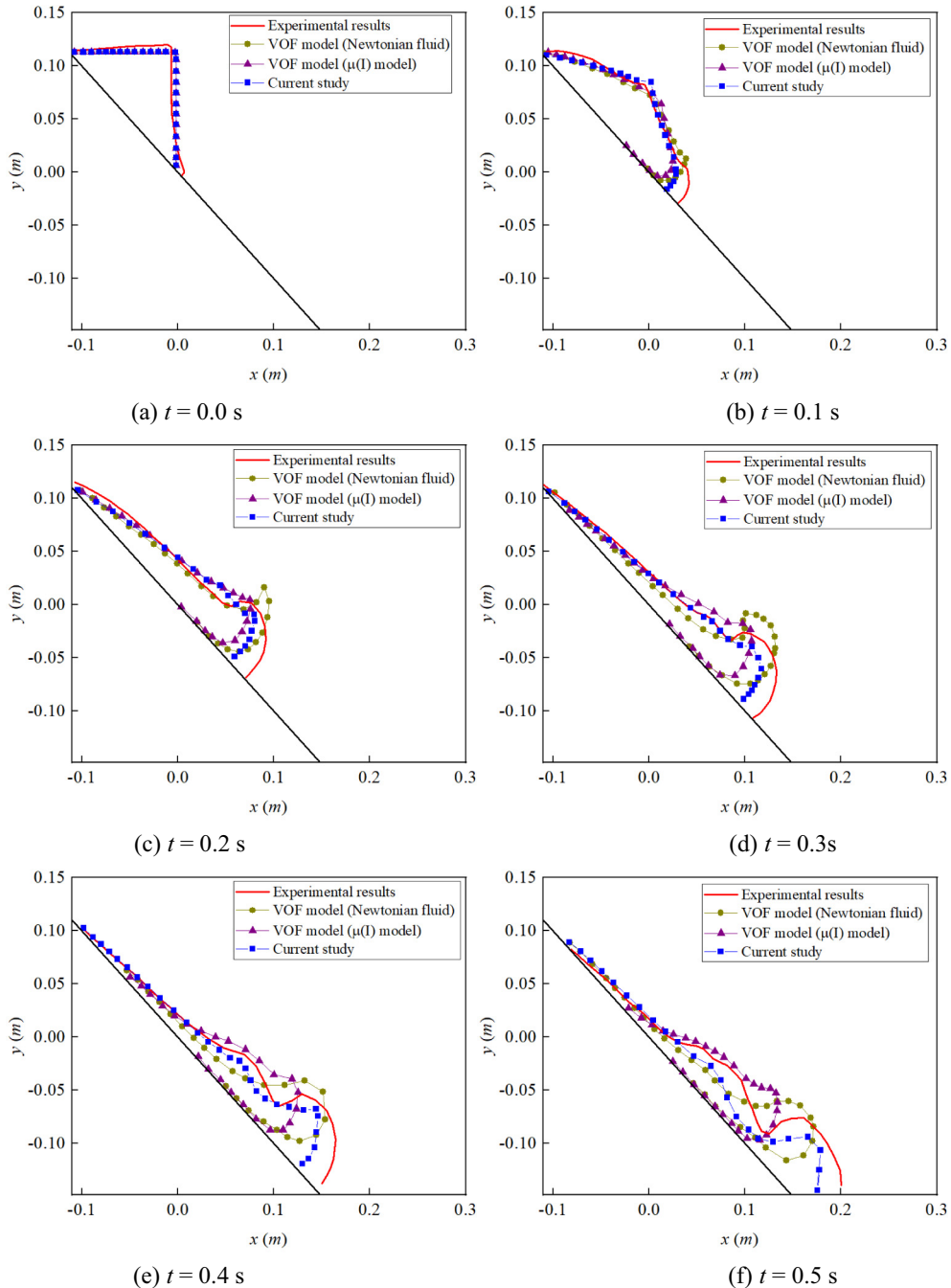


Fig. 18. Comparison of the profiles of the granular landslides of the experiment data [102] and the numerical results calculated by the proposed method and by Clous and Abadie [107] with different rheological model (Newtonian fluid and $\mu(I)$ model) at (a) $t = 0.0$ s, (b) $t = 0.1$ s, (c) $t = 0.2$ s, (d) $t = 0.3$ s, (e) $t = 0.4$ s, (f) $t = 0.5$ s.

the ambient fluid around granular landslides. However, very satisfactory results are observed in terms of impulse wave frequencies.

5. Conclusion

A multi-phase WCPH method based on the $\mu(I)$ rheological model was developed for modeling sub-aerial, submerged, and dry granular landslides. In this paper, some advanced numerical techniques of single-phase SPH are modified and introduced into multi-phase WCPH to improve its performance in granular flow problems. These improvements include: (i) The incremental diffusive term $D^{\delta m-SPH}$ of the multi-phase granular flows is developed by adopting the form of density increment. Compared with the traditional diffusive term,

which significantly improves the smoothness and stability of the pressure field near the boundary and phase interface. (ii) The PST for the multi-phase WCPH model is developed by adopting the two-step shifting method to ensure the uniform distribution of particles in each phase and phase interface in the simulation process. (iii) A dynamic effective pressure calculation method is introduced, which dynamically calculates the pore water pressure through the equation of state to avoid the error caused by phase interface search. (iv) A general friction boundary condition is introduced. The algorithm is implemented based on the momentum exchange between the boundary surface and the deposited particles. The case of submerged landslides shows that the friction boundary conditions adopted in this work are suitable for the simulation of granular landslides. The

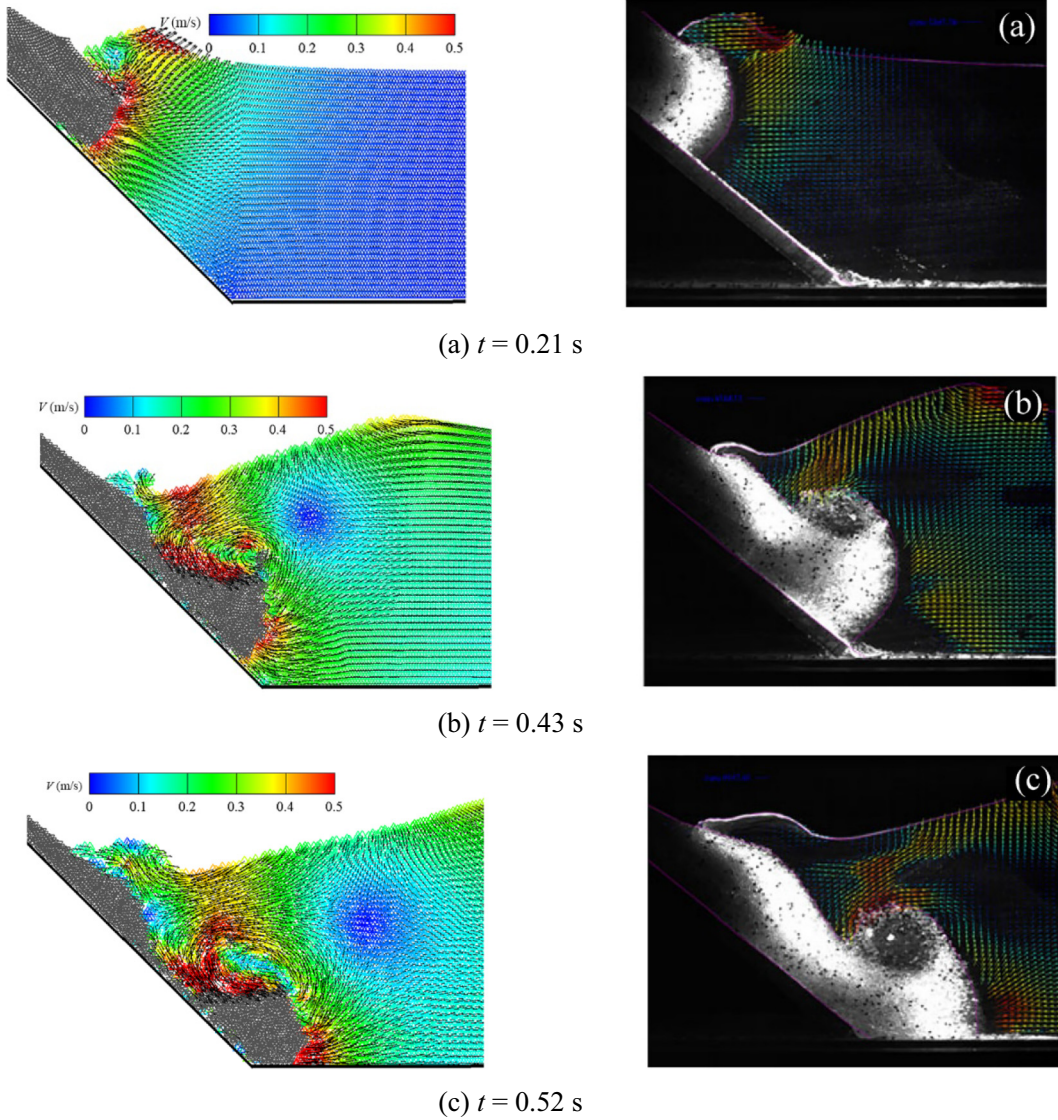


Fig. 19. Comparison of numerical simulation and experimental snapshot [102] of waves produced by sub-aerial granular landslides at: (a) $t = 0.21$ s, (b) $t = 0.43$ s, (c) $t = 0.52$ s.

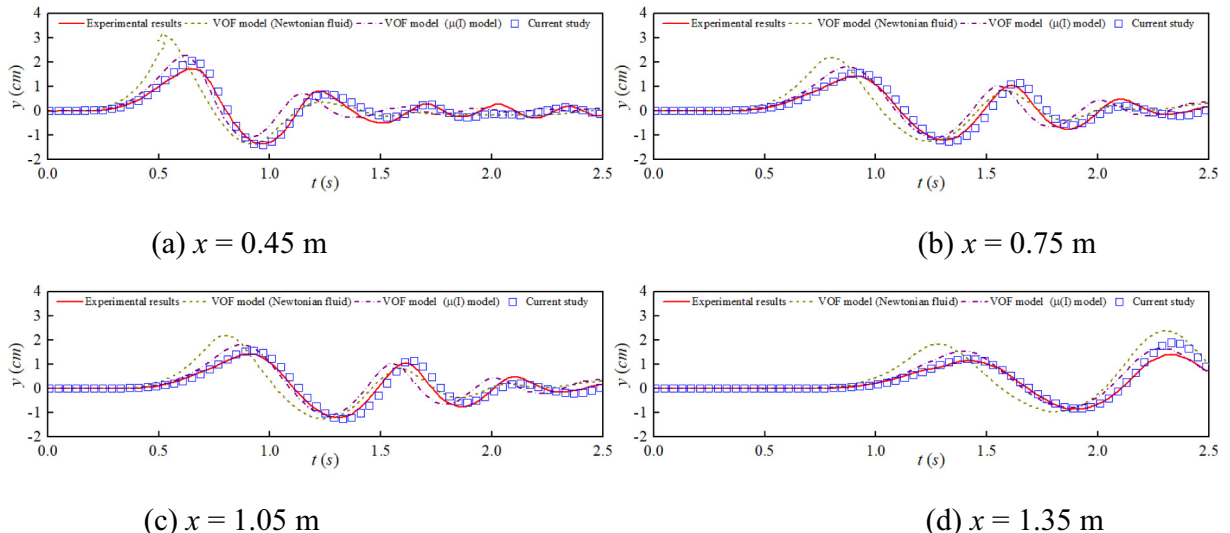


Fig. 20. Free water surface profiles versus time obtained by the proposed model and Clous and Abadie [107] at different water elevation gauges and compared with experimental data.

results are closer to experimental data than methods that do not consider basal friction.

The model was validated and evaluated by two phases hydrostatic stratified column, rigid landslide, sub-aerial, submerged, and dry granular landslides, and compared with the experimental result and previous numerical methods. The verification for the two phases hydrostatic stratified column showed that the $D^{\delta m-SPH}$ can effectively eliminate the non-physical fluctuation of the pressure field of multi-phase flows. The verifications of deformable landslides (sub-aerial, submerged, and dry) showed that the results of the developed multi-phase WCSPH model well agree with the experimental results. Compared with past studies, the model in this paper has a remarkable improvement in predicting the evolution of granular landslides and the induced impulse waves, especially sub-aerial granular landslides. Overall, the multi-phase WCSPH method showed more robust performance and practicability in landslide surge problems.

Declaration of Competing Interest

The authors declare that they have no known competing financial interests or personal relationships that could have appeared to influence the work reported in this paper.

Acknowledgements

This study was supported by the National Natural Science Foundation of China (No. 52079025) and the National Natural Science Foundation of China (No. 52031002).

References

- [1] E. Jafari Nodoushan, A. Shakibaenia, K. Hosseini, A multiphase meshfree particle method for continuum-based modeling of dry and submerged granular flows, *Powder Technol.* 335 (2018) 258–274.
- [2] L. Fu, Y.-C. Jin, Investigation of non-deformable and deformable landslides using meshfree method, *Ocean Eng.* 109 (2015) 192–206.
- [3] K.T. Ramadan, M.A. Omar, A.A. Allam, Modeling of tsunami generation and propagation under the effect of stochastic submarine landslides and slumps spreading in two orthogonal directions, *Ocean Eng.* 75 (2014) 90–111.
- [4] P. Lynett, P.L.F. Liu, A numerical study of submarine-landslide-generated waves and run-up, *Proceedings of the Royal Society of London. Series A: Mathematical, Physical and Engineering Sciences*, vol. 458, 2002, pp. 2885–2910.
- [5] S.A. Rzadkiewicz, C. Mariotti, P. Heinrich, Numerical simulation of submarine landslides and their hydraulic effects, *J. Waterw. Port. C ASCE* 123 (1997) 149–157.
- [6] B.H. Keating, W.J. McGuire, Island edifice failures and associated tsunami hazards, *Pure Appl. Geophys.* 157 (2000) 899–955.
- [7] H. Shi, P. Si, P. Dong, X. Yu, A two-phase SPH model for massive sediment motion in free surface flows, *Adv. Water Resour.* 129 (2019) 80–98.
- [8] M. Tajnesiae, A. Shakibaenia, K. Hosseini, Meshfree particle numerical modelling of sub-aerial and submerged landslides, *Comput. Fluids* 172 (2018) 109–121.
- [9] C.T. Nguyen, C.T. Nguyen, H.H. Bui, G.D. Nguyen, R. Fukagawa, A new SPH-based approach to simulation of granular flows using viscous damping and stress regularisation, *Landslides* 14 (2016) 69–81.
- [10] A. Armanini, M. Larcher, E. Nucci, M. Dumbser, Submerged granular channel flows driven by gravity, *Adv. Water Resour.* 63 (2014) 1–10.
- [11] L. Lacaze, J.C. Phillips, R.R. Kerswell, Planar collapse of a granular column: experiments and discrete element simulations, *Phys. Fluids* 20 (2008).
- [12] P.Y. Lagrée, L. Staron, S. Popinet, The granular column collapse as a continuum: validity of a two-dimensional Navier-Stokes model with a $\mu(I)$ -rheology, *J. Fluid Mech.* 686 (2011) 378–408.
- [13] I.R. Ionescu, A. Mangeney, F. Bouchut, O. Roche, Viscoplastic modeling of granular column collapse with pressure-dependent rheology, *J. Non-Newtonian Fluid Mech.* 219 (2015) 1–18.
- [14] R.A. Gingold, J.J. Monaghan, Smoothed particle hydrodynamics - theory and application to non-spherical stars, *Mon. Not. R. Astron. Soc.* 181 (1977) 375–389.
- [15] S. Koshizuka, Y. Oka, Moving-particle semi-implicit method for fragmentation of incompressible fluid, *Nucl. Sci. Eng.* 123 (1996) 421–434.
- [16] L.B. Lucy, A numerical approach to the testing of the fission hypothesis, *Astrophys. J.* 8 (1977) 1013–1024.
- [17] J.J. Monaghan, Simulating free surface flows with SPH, *J. Comput. Phys.* 110 (1994) 399–406.
- [18] T. Long, D. Hu, D.T. Wan, C. Zhuang, G. Yang, An arbitrary boundary with ghost particles incorporated in coupled FEM-SPH model for FSI problems, *J. Comput. Phys.* 350 (2017) 166–183.
- [19] A. Khayyer, H. Gotoh, H. Falahaty, Y. Shimizu, An enhanced ISPH-SPH coupled method for simulation of incompressible fluid–elastic structure interactions, *Comput. Phys. Commun.* 232 (2018) 139–164.
- [20] M. Liu, Z. Zhang, Smoothed particle hydrodynamics (SPH) for modeling fluid-structure interactions, *science China physics, Mech. Astron.* 62 (2019).
- [21] G. Oger, A. Vergnaud, B. Bouscasse, J. Ohana, M. Abu Zarim, M. De Leffe, A. Bannier, L. Chiron, Y. Jus, M. Garnier, S. Halbout, D. Le Touzé, Simulations of helicopter ditching using smoothed particle hydrodynamics, *J. Hydraul.* 32 (2020) 653–663.
- [22] C. Tsurudome, D. Liang, Y. Shimizu, A. Khayyer, H. Gotoh, Incompressible SPH simulation of solitary wave propagation on permeable beaches, *J. Hydraul.* 32 (2020) 664–671.
- [23] W.-J. Xu, X.-Y. Dong, Simulation and verification of landslide tsunamis using a 3D SPH-DEM coupling method, *Comput. Geotech.* 129 (2021).
- [24] A.M. Zhang, P.N. Sun, F.R. Ming, A. Colagrossi, Smoothed particle hydrodynamics and its applications in fluid-structure interactions, *J. Hydraul.* 29 (2017) 187–216.
- [25] A. Tafuni, J.M. Domínguez, R. Vacondio, A.J.C. Crespo, A versatile algorithm for the treatment of open boundary conditions in smoothed particle hydrodynamics GPU models, *Comput. Method Appl. M* 342 (2018) 604–624.
- [26] P.N. Sun, A. Colagrossi, S. Marrone, M. Antuono, A.M. Zhang, Multi-Resolution Delta-plus-SPH with tensile instability control: towards high Reynolds number flows, *Comput. Phys. Commun.* 224 (2018) 63–80.
- [27] X. Zheng, S.D. Shao, A. Khayyer, W.Y. Duan, Q.W. Ma, K.P. Liao, Corrected first-order derivative ISPH in water wave simulations, *Coast. Eng. J.* 59 (2017).
- [28] P.N. Sun, D. Le Touzé, A.M. Zhang, Study of a complex fluid-structure dam-breaking benchmark problem using a multi-phase SPH method with APR, *Eng. Anal. Bound. Elem.* 104 (2019) 240–258.
- [29] K. Hosseini, P. Omidvar, M. Kheirkhahan, S. Farzin, Smoothed particle hydrodynamics for the interaction of Newtonian and non-Newtonian fluids using the $\mu(I)$ model, *Powder Technol.* 351 (2019) 325–337.
- [30] M. Kheirkhahan, P. Omidvar, K.H. Hosseini, Effective pressure for two phase water-sediment models using SPH method, *J. Appl. Fluid Mech.* 13 (2020) 1193–1206.
- [31] A. Krimi, S. Khelladi, X. Nogueira, M. Deligant, R. Ata, M. Rezoug, Multiphase smoothed particle hydrodynamics approach for modeling soil–water interactions, *Adv. Water Resour.* 121 (2018) 189–205.
- [32] B. Ataei-Ashtiani, G. Shobeyri, Numerical simulation of landslide impulsive waves by incompressible smoothed particle hydrodynamics, *Int. J. Numer. Meth. Fl.* 56 (2008) 209–232.
- [33] G. Pahar, A. Dhar, Coupled incompressible smoothed particle hydrodynamics model for continuum-based modelling sediment transport, *Adv. Water Resour.* 102 (2017) 84–98.
- [34] M. Khanpour, A.R. Zarrati, M. Kolahdoozan, A. Shakibaenia, S.M. Amirshahi, Mesh-free SPH modeling of sediment scouring and flushing, *Comput. Fluids* 129 (2016) 67–78.
- [35] Q. Ran, J. Tong, S. Shao, X. Fu, Y. Xu, Incompressible SPH scour model for movable bed dam break flows, *Adv. Water Resour.* 82 (2015) 39–50.
- [36] M. Kheirkhahan, K. Hosseini, Comparison of the $\mu(I)$ and HBP models for simulating granular media, *Int. J. Modern Phys. C* 29 (2018).
- [37] P. Jop, Y. Forterre, O. Pouliquen, A constitutive law for dense granular flows, *Nature* 441 (2006) 727–730.
- [38] M. Jandaghian, A. Krimi, A. Shakibaenia, Enhanced weakly-compressible MPS method for immersed granular flows, *Adv. Water Resour.* 152 (2021).
- [39] É. Guazzelli, O. Pouliquen, Rheology of dense granular suspensions, *J. Fluid Mech.* 852 (2018).
- [40] H.F. Schwaiger, B. Higman, Lagrangian hydrocode simulations of the 1958 Lituya Bay tsunamigenic rockslide, *Geochim. Geophys. Geosyst.* 8 (2007) n/a–n/a.
- [41] C. Shi, Y. An, Q. Wu, Q. Liu, Z. Cao, Numerical simulation of landslide-generated waves using a soil–water coupling smoothed particle hydrodynamics model, *Adv. Water Resour.* 92 (2016) 130–141.
- [42] K. Szewc, Smoothed particle hydrodynamics modeling of granular column collapse, *Granul. Matter* 19 (2016).
- [43] A.S. Baumgarten, K. Kamrin, A general fluid–sediment mixture model and constitutive theory validated in many flow regimes, *J. Fluid Mech.* 861 (2018) 721–764.
- [44] G.D.R. MiDi, On dense granular flows, *Eur. Phys. J. E. Soft. Matter.* 14 (2004) 341–365.
- [45] F. da Cruz, S. Emam, M. Prochnow, J.N. Roux, F. Chevoir, Rheophysics of dense granular materials: discrete simulation of plane shear flows, *Phys. Rev. E Stat. Nonlinear Soft Matter Phys.* 72 (2005), 021309.
- [46] L. Staron, P.Y. Lagrée, S. Popinet, The granular silo as a continuum plastic flow: the hour-glass vs the clepsydra, *Phys. Fluids* 24 (2012).
- [47] J. Chauchat, M. Médale, A three-dimensional numerical model for dense granular flows based on the $\mu(I)$ rheology, *J. Comput. Phys.* 256 (2014) 696–712.
- [48] E.J. Nodoushan, A. Shakibaenia, Multiphase mesh-free particle modeling of local sediment scouring with $\mu(I)$ rheology, *J. Hydroinf.* 21 (2019) 279–294.
- [49] L. Ke, Y.-C. Jin, T. Xu, Y.-C. Tai, Investigating the physical characteristics of dense granular flows by coupling the weakly compressible moving particle semi-implicit method with the rheological model, *Acta Geotech.* 15 (2020) 1815–1830.
- [50] A. Ghaitanellis, D. Violeau, M. Ferrand, K.E.K. Abderrezak, A. Leroy, A. Joly, A SPH elastic-viscoplastic model for granular flows and bed-load transport, *Adv. Water Resour.* 111 (2018) 156–173.
- [51] E.H. Zubeldia, G. Fourtakas, B.D. Rogers, M.M. Farias, Multi-phase SPH model for simulation of erosion and scouring by means of the shields and Drucker–Prager criteria, *Adv. Water Resour.* 117 (2018) 98–114.
- [52] G. Fourtakas, B.D. Rogers, Modelling multi-phase liquid-sediment scour and resuspension induced by rapid flows using smoothed particle hydrodynamics (SPH) accelerated with a graphics processing unit (GPU), *Adv. Water Resour.* 92 (2016) 186–199.
- [53] J. Monaghan, Smoothed particle hydrodynamics, *Annu. Rev. Astron. Astrophys.* 30 (1992) 543–574.

- [54] M. Antuono, A. Colagrossi, S. Marrone, D. Molteni, Free-surface flows solved by means of SPH schemes with numerical diffusive terms, *Comput. Phys. Commun.* 181 (2010) 532–549.
- [55] P.N. Sun, A. Colagrossi, S. Marrone, A.M. Zhang, The δ -plus-SPH model: simple procedures for a further improvement of the SPH scheme, *Comput. Method Appl. M* 315 (2017) 25–49.
- [56] A. Krimi, M. Jandaghian, A. Shakibaeinia, A WCSPH particle shifting strategy for simulating violent free surface flows, *Water* 12 (2020).
- [57] T. Xu, Y.-C. Jin, Improvements for accuracy and stability in a weakly-compressible particle method, *Comput. Fluids* 137 (2016) 1–14.
- [58] G. Fournakis, J.M. Dominguez, R. Vacdindio, B.D. Rogers, Local uniform stencil (LUST) boundary condition for arbitrary 3-D boundaries in parallel smoothed particle hydrodynamics (SPH) models, *Comput. Fluids* 190 (2019) 346–361.
- [59] B.X. Zheng, Z. Chen, A multiphase smoothed particle hydrodynamics model with lower numerical diffusion, *J. Comput. Phys.* 382 (2019) 177–201.
- [60] B. Sheikh, T. Qiu, A. Ahmadipour, Comparison of SPH boundary approaches in simulating frictional soil–structure interaction, *Acta Geotech.* 16 (2020) 2389–2408.
- [61] X. Zhang, K. Krabbenhoft, D. Sheng, Particle finite element analysis of the granular column collapse problem, *Granul. Matter* 16 (2014) 609–619.
- [62] X. Zhang, Y. Ding, D. Sheng, S.W. Sloan, W. Huang, Quasi-static collapse of two-dimensional granular columns: insight from continuum modelling, *Granul. Matter* 18 (2016).
- [63] R. Gutfraind, S.B. Savage, Smoothed particle hydrodynamics for the simulation of broken-ice fields: Mohr–coulomb-type rheology and frictional boundary conditions, *J. Comput. Phys.* 134 (1997) 203–215.
- [64] J. Wang, D. Chan, Frictional contact algorithms in SPH for the simulation of soil–structure interaction, *Int. J. Numer. Anal. Methods Geomech.* 38 (2014) 747–770.
- [65] A. Shakibaeinia, Y.C. Jin, A weakly compressible MPS method for modeling of open-boundary free-surface flow, *Int. J. Numer. Meth. Fl.* 63 (2010) 1208–1232.
- [66] S. Marrone, M. Antuono, A. Colagrossi, G. Colicchio, D. Le Touze, G. Graziani, delta-SPH model for simulating violent impact flows, *Comput. Method Appl. M* 200 (2011) 1526–1542.
- [67] P. Sun, F. Ming, A. Zhang, Numerical simulation of interactions between free surface and rigid body using a robust SPH method, *Ocean Eng.* 98 (2015) 32–49.
- [68] W. Dehnen, H. Aly, Improving convergence in smoothed particle hydrodynamics simulations without pairing instability, *Mon. Not. R. Astron. Soc.* 425 (2012) 1068–1082.
- [69] H. Wendland, Piecewise polynomial, positive definite and compactly supported radial functions of minimal degree, *Adv. Comput. Math.* 4 (1995) 389–396.
- [70] D. Molteni, A. Colagrossi, A simple procedure to improve the pressure evaluation in hydrodynamic context using the SPH, *Comput. Phys. Commun.* 180 (2009) 861–872.
- [71] D.D. Meringolo, F. Aristodemo, P. Veltre, SPH numerical modeling of wave-perforated breakwater interaction, *Coast. Eng.* 101 (2015) 48–68.
- [72] M.D. Green, J. Peiró, Long duration SPH simulations of sloshing in tanks with a low fill ratio and high stretching, *Comput. Fluids* 174 (2018) 179–199.
- [73] M. Antuono, S. Marrone, A. Colagrossi, Violent wave impacts and loadings using the δ -SPH method, advanced numerical modelling of wave structure, *Interactions* (2021) 121–147.
- [74] X.Y. Hu, N.A. Adams, An incompressible multi-phase SPH method, *J. Comput. Phys.* 227 (2007) 264–278.
- [75] D.D. Meringolo, Y. Liu, X.-Y. Wang, A. Colagrossi, Energy balance during generation, propagation and absorption of gravity waves through the δ -LES-SPH model, *Coast. Eng.* 140 (2018) 355–370.
- [76] A. Di Mascio, M. Antuono, A. Colagrossi, S. Marrone, Smoothed particle hydrodynamics method from a large eddy simulation perspective, *Phys. Fluids* 29 (2017), 035102.
- [77] Y. Forterre, O. Pouliquen, Flows of dense granular media, *Annu. Rev. Fluid Mech.* 40 (2008) 1–24.
- [78] C. Cassar, M. Nicolas, O. Pouliquen, Submarine granular flows down inclined planes, *Phys. Fluids* 17 (2005).
- [79] M. Pilvar, M.J. Pouraghniaei, A. Shakibaeinia, Two-dimensional sub-aerial, submerged, and transitional granular slides, *Phys. Fluids* 31 (2019).
- [80] T. Papanastasiou, Flow material with yield, *J. Rheol.* 31 (1987).
- [81] S. Bandara, K. Soga, Coupling of soil deformation and pore fluid flow using material point method, *Comput. Geotech.* 63 (2015) 199–214.
- [82] C. Huang, D.H. Zhang, Y.X. Shi, Y.L. Si, B. Huang, Coupled finite particle method with a modified particle shifting technology, *Int. J. Numer. Methods Eng.* 113 (2018) 179–207.
- [83] R. Xu, P. Stansby, D. Laurence, Accuracy and stability in incompressible SPH (ISPH) based on the projection method and a new approach, *J. Comput. Phys.* 228 (2009) 6703–6725.
- [84] S.J. Lind, R. Xu, P.K. Stansby, B.D. Rogers, Incompressible smoothed particle hydrodynamics for free-surface flows: a generalised diffusion-based algorithm for stability and validations for impulsive flows and propagating waves, *J. Comput. Phys.* 231 (2012) 1499–1523.
- [85] A. Khayyer, H. Gotoh, Y. Shimizu, Comparative study on accuracy and conservation properties of two particle regularization schemes and proposal of an optimized particle shifting scheme in ISPH context, *J. Comput. Phys.* 332 (2017) 236–256.
- [86] P.-P. Wang, Z.-F. Meng, A.M. Zhang, F.-R. Ming, P.-N. Sun, Improved particle shifting technology and optimized free-surface detection method for free-surface flows in smoothed particle hydrodynamics, *Comput. Method Appl. M* 357 (2019).
- [87] A. Khayyer, H. Gotoh, Y. Shimizu, A projection-based particle method with optimized particle shifting for multiphase flows with large density ratios and discontinuous density fields, *Comput. Fluids* 179 (2019) 356–371.
- [88] M. Antuono, A. Colagrossi, S. Marrone, Numerical diffusive terms in weakly-compressible SPH schemes, *Comput. Phys. Commun.* 183 (2012) 2570–2580.
- [89] J.J. Monaghan, Smoothed particle hydrodynamics, *Rep. Prog. Phys.* 68 (2005) 1703–1759.
- [90] S. Adami, X.Y. Hu, N.A. Adams, A generalized wall boundary condition for smoothed particle hydrodynamics, *J. Comput. Phys.* 231 (2012) 7057–7075.
- [91] J.J. Monaghan, SPH without a tensile instability, *J. Comput. Phys.* 159 (2000) 290–311.
- [92] T. Capone, A. Panizzo, J.J. Monaghan, SPH modelling of water waves generated by submarine landslides, *J. Hydraul. Res.* 48 (2010) 80–84.
- [93] P.Z. Lin, X. Liu, J.M. Zhang, The simulation of a landslide-induced surge wave and its overtaking of a dam using a coupled ISPH model, *Eng. Appl. Comput. Fluid Mech.* 9 (2015) 432–444.
- [94] S. Yeylaghi, B. Moa, B. Buckingham, P. Oshkai, J. Vasquez, C. Crawford, ISPH modelling of landslides generated waves for rigid and deformable slides in Newtonian and non-Newtonian reservoir fluids, *Adv. Water Resour.* 107 (2017) 212–232.
- [95] H. Tan, Q. Xu, S.H. Chen, Subaerial rigid landslide-tsunamis: insights from a block DEM-SPH model, *Eng. Anal. Bound. Elem.* 95 (2018) 297–314.
- [96] P. Heinrich, Nonlinear water waves generated by submarine and aerial landslides, *Journal of waterway, port, coastal, and ocean engineering* 118 (1992) 249–266.
- [97] S. Abadie, D. Morichon, S. Grilli, S. Glockner, Numerical simulation of waves generated by landslides using a multiple-fluid Navier-Stokes model, *Coast. Eng.* 57 (2010) 779–794.
- [98] G. Zhang, J. Chen, Y. Qi, J. Li, Q. Xu, Numerical simulation of landslide generated impulse waves using a δ -LES-SPH model, *Adv. Water Resour.* 151 (2021).
- [99] S.T. Grilli, M. Shelby, O. Kimmoun, G. Dupont, D. Nicolsky, G. Ma, J.T. Kirby, F. Shi, Modeling coastal tsunami hazard from submarine mass failures: effect of slide rheology, experimental validation, and case studies off the US East Coast, *Nat. Hazards* 86 (2016) 353–391.
- [100] M.-L. Yu, C.-H. Lee, Multi-phase-flow modeling of underwater landslides on an inclined plane and consequently generated waves, *Adv. Water Resour.* 133 (2019).
- [101] A. Ghaitanellis, Modelling Bed-Load Sediment Transport through a Granular Approach in SPH, 2017.
- [102] S. Viroulet, A. Sauret, O. Kimmoun, C. Kharif, Granular collapse into water: toward tsunami landslides, *J. Vis.* 16 (2013) 189–191.
- [103] S. Viroulet, A. Sauret, O. Kimmoun, Tsunami generated by a granular collapse down a rough inclined plane, *EPL (Europhys. Lett.)* 105 (2014).
- [104] P. Jop, Y. Forterre, O. Pouliquen, Crucial role of sidewalls in granular surface flows: consequences for the rheology, *J. Fluid Mech.* (2005) 167–192.
- [105] P. Jop, Y. Forterre, O. Pouliquen, A constitutive law for dense granular flows, *Nature* 441 (7094) (2006) 727–730.
- [106] T. Xu, Y.C. Jin, Modeling free-surface flows of granular column collapses using a mesh-free method, *Powder Technol.* 291 (2016) 20–34.
- [107] L. Clous, S. Abadie, Simulation of energy transfers in waves generated by granular slides, *Landslides* 9 (2019).